Simplified Li-ion cell model for BMS coupling an equivalent-circuit dynamic model with a zero-dimensional physics-based SEI model

D. García Elvira[1z], R. Machado[2], G.L. Plett[2], M.S. Trimboli[2], H. Valderrama Blavi[1], A. Cid Pastor[1], L. Martínez Salamero[1]

[1] Universitat Rovira i Virgili (URV). Tarragona, 43007, Spain.

[2] University of Colorado Colorado Springs (UCCS). Colorado Springs, CO 809018, United States.

[z] Corresponding author. Email address [david.garciae@urv.cat]

ABSTRACT

This paper presents a computationally simple degradation model of a Lithium Nickel Manganese Cobalt Oxide (NMC) battery cell with graphite negative electrode, intended for Battery Management System (BMS) controls. The proposed model combines the simplicity of an equivalent circuit, which explains the fast dynamics of the cell, with a zero-dimensional physics-based model of Solid Electrolyte Interphase (SEI) growth, which predicts long-term capacity loss and internal resistance rise. The SEI reaction involves loss of lithium inventory, which produces a relative displacement between the negative and the positive electrodes' stoichiometric windows. This, in turn, modifies the cell's Open Circuit Voltage (OCV) curve. Since the electrodes' lithiation boundaries are defined for the modeled cell by voltage limits, the modification of the OCV curve causes a secondary capacity recovery. The reason is that, after degradation, a fraction of the previously unused lithium reserves of both electrodes needs to be incorporated into the cyclable lithium range to reach the OCV limits. The proposed model quantifies this process to fine-tune the capacity loss prediction. The simulation results suggest that a reversible mechanism may be taking place alongside SEI growth, causing voltage drop during self-discharge without reducing the cell's lithium inventory.

Keywords. – Equivalent-Circuit Model, Capacity Fade Model, Solid Electrolyte Interphase, SEI Degradation, Shift of Open Circuit Potential Curves, Secondary Capacity Recovery.

INTRODUCTION

Studying lithium-ion battery degradation is essential to extend their lifetime in applications such as microgrids and electric vehicles. [1–3]. As batteries age, their power and storage capacity decrease and their internal resistance increases. Understanding and modeling degradation processes is key to developing precise algorithms to estimate State of Charge (SOC) and available power and energy. In addition, degradation models make possible to perform predictive control aimed at maximizing battery life. Next generation Battery Management Systems (BMS) are expected to integrate battery models to make intelligent decisions that prolong battery life ("aging management") [4].

Scope of the paper. – The purpose of this work is to develop a computationally simple cell model of dynamics and aging that could be used by BMS algorithms to estimate the degree of aging that would be experienced by a battery cell under different possible future control actions. This would allow the BMS to decide what would be an acceptable future control action that would prevent premature aging of the cells.

Battery cell modeling. – In accordance with [5], the two most employed battery model types are equivalent-circuit models and physics-based models. On one hand, equivalent-circuit models are simple and require little computational power. However, this type of model lacks long-term predictive capability; that is, circuit models do not provide information on how the cell will behave as it ages. On the other hand, physics-based models are much more complex but, in return, they are more versatile and allow estimation of cell degradation. This paper couples an equivalent-circuit model with a reduced-order physics-based model of one of the dominant degradation mechanisms in lithium-ion cells with graphite negative electrode, Solid Electrolyte Interphase (SEI) growth.

SEI layer growth. – In lithium-ion batteries, the electrodes operate at potentials outside of the thermodynamic stability limits of the electrolyte to maximize energy storage [2]. This causes an SEI layer to form at the interface between electrode and electrolyte, decomposing the latter. The SEI layer initially passivates the negative electrode surface, which prevents parasitic reactions and kinetically stabilizes the system [6]. During the initial cycles, 10% of the original capacity is generally consumed in irreversible SEI formation (irreversible capacity loss) in the anode [7]. Lithium ion cells are generally assembled with fully lithiated positive electrode (PE) and fully de-lithiated negative electrode (NE). Thus, lithium consumed in the formation process comes from the positive electrode. Pre-lithiation of the positive or the negative electrode, utilization of electrode coatings, and utilization of electrolyte additives can help forming an optimized SEI layer on the initial cycling [8–10]. An optimized SEI layer is expected to have negligible electronic conductivity and high electrolyte diffusion resistance while having high lithium-ion selectivity and permeability [7].

Right after the formation cycle the usable capacity of both electrodes is balanced [11]. Afterwards, the negative electrode generally limits the cell capacity (due to SEI growth and lithium plating, among other mechanisms). SEI layer growth in graphite NEs is generally regarded as a dominant degradation mechanism [12–17]. The SEI layer continues to grow throughout the lifetime of the cell. Indeed, after the initial passivation of the NE, the electrolyte still diffuses through the porous SEI layer and keeps reacting at the electrode's surface [18], consuming cyclable lithium in the reduction reaction, especially with low NE's potential –i.e. high SOC. This happens at an ever-slowing rate as the thickness of the SEI layer increases. The SEI reaction is thus self-limiting but the reaction never fully stops [14]. In calendar aging, the main degradation mechanism is the loss of lithium inventory caused by SEI layer growth [19]. However, the majority of SEI layer growth occurs during the charging stage of cycling [20]. The proposed model accounts for both calendar and cycling aging caused by SEI growth.

Proposed model. – An incremental (discrete time) model combining an equivalent-circuit model with a reduced-order physics-based model is presented in this paper. The base of the model is the Enhanced Self Correcting (ESC) equivalent-circuit model [5]. Time dependency has been introduced into some

of the parameters to account for degradation. These time-dependent parameters are updated by incorporating changes in the cell's capacity and internal resistance, which are predicted by a reduced-order physics-based model of the SEI side reaction [18, 21]. Therefore, the proposed model combines the simplicity of the equivalent circuit with the long-term prediction capability of the physics-based model.

The cells studied in this work were manufactured by Panasonic; they have prismatic form factor, Nickel Manganese Cobalt Oxide (NMC) positive electrode, graphite negative electrode, and liquid electrolyte containing ethylene carbonate organic solvent. These cells were used in the battery packs of the Ford C-MAX Energi and Ford Fusion Energi plug-in hybrid vehicles (PHEVs) between 2013 and 2018. Their nominal voltage is 3.7 V and their nominal capacity is 25 Ah. They are commercial cells which physical characteristics are not publicly known since they are part of the manufacturer trade secrets. The characterization of this cell type has been addressed in recent works [22–24].

Relevance of the paper. – A BMS-oriented model must be computationally simple. Full order physics-based models are highly accurate but they are not implementable in a microcontroller for real-time applications due to their complexity [4, 25, 26]. Simplifying such models leads to deriving reduced-order models which intend to preserve the accuracy of the full-order model, while reducing the computational effort required to perform the calculations. In [27], a reduced-order model was derived using the state space method and linearization achieving a computational performance of approximately $2\,ms$ per second of actual operation, reporting $13\,mV$ weighted normalized error approximately. However, no degradation mechanism was modeled. In [28], an equivalent-circuit model was derived from a pseudo-two dimensional electrochemical-thermal model achieving computational performance of approximately $50\,ms$ per second of actual operation with a root mean squared (RMS) voltage error of $29\,mV$. In [26], the effect in performance and computational time of several model simplifications and numerical methods is evaluated, the fastest of which attains $0.2\,ms$ per real-time second, with $17\,mV$ error. Battery aging was not modeled in this study. In [16], various degradation models from literature (included that of Randall et al. [18]) were implemented within a single particle model framework and their performance compared. However, no error metrics or computational times were provided. In [29], a full-order electrochemical model was extended by adding models of several degradation mechanisms (SEI growth, lithium platting, electrolyte dissolution, loss of active material…), resulting in $740\,ms$ computational time per real-time second. The proposed model takes approximately six minutes to simulate seven months of cell operation, using MatlabR2021a in Intel® Core™ i7-6700 CPU @ 4.40 GHz, 16 GB RAM. Therefore, it takes less than $0.02\,ms$ to compute the result of one second of actual operation (that is one order of magnitude faster than the reviewed physics-based reduced-order models), and the voltage error observed in simulations is $28.7\,mV$ (same order of magnitude compared to physics-based reduced-order models).

A thorough search of the relevant literature has yielded few references that resemble the work proposed here of coupling an equivalent-circuit model with a physics-based model. The most similar works found are [30, 31], in which equivalent-circuit models were derived from physical variables, assigning actual physical meaning to the passive electrical circuit elements. In [30], a pseudo-two-dimensional physics-based model was considered and the resulting equivalent-circuit model was not coupled with an aging

mechanism. In [31], a single-particle physics-based model was selected as the base of the simplified model and SEI growth was considered to model cell degradation. The resulting model was intended for system-level design and planning studies. The model proposed here is the first-ever published work, to the best of the author's knowledge, that couples an empirically derived equivalent-circuit model with a reduced-order physics-based degradation model of SEI growth to obtain a simplified incremental model intended for BMS that exhibits high computational speed. The proposed model can be used for implementing preventive control, in order to extend battery life.

In addition, several improvements to the original formulation of the SEI degradation model employed have been developed:

- Modeling secondary capacity recovery (which was not addressed in [18, 21]) to fine-tune the capacity fade estimation.
- Estimating SOC electrochemically, from the degree of lithiation of the electrodes rather than from coulomb counting.
- Reducing computational time by pre-storing the degradation model results obtained for a variety of operation conditions.

Simulation results reveal differences between predicted and measured voltage over prolonged self-discharge periods. These differences show a certain pattern that suggests that, additionally to SEI growth, there is a second mechanism that produces voltage drop in the unloaded cell at high SOC. The process is reversible because it causes loss of charge without causing loss of lithium inventory. This finding has inspired ongoing research to model the process as the consequence of a small-magnitude electrochemical internal short circuit.

Work limitations. – This work assumes fresh cells after the formation cycles, i.e. the proposed model does not cover loss of lithium in the initial charging/discharging cycles, but subsequent growth of the SEI layer only. Literature often distinguishes between two factors that are considered when modeling the SEI rate of growth [32]. This rate may be considered to be limited by the maximum speed of the reaction between the electrolyte solvent and the graphite NE (this is known as a "kinetics-limited" model), or the rate may be limited by the ability of solvent molecules to diffuse through the SEI layer to the surface of the NE (this is known as a "diffusion-limited" model). In this paper, a simple kinetics-limited model based on [18, 21, 33] is considered. Future work will address the generalization of this result to also consider a diffusion-limited model based on [32, 34].

It should be noted that there are many other causes of degradation that affect lithium-ion batteries apart from SEI growth [12, 16]. These have not been considered in the proposed model, although upgrading to more comprehensive models is an interesting topic of future research.

Finally, testing the proposed model in a BMS is beyond the scope of the paper and is the subject of proposed future work.

Additional degradation mechanisms. – Together with SEI growth, mechanical stress and lithium plating are also among the most important degradation mechanisms, although they have not been modeled here. They are briefly reviewed next following [16, 35, 36]:

- Mechanical stress: Lithium intercalation causes most electrode materials to expand and lithium deintercalation causes them to contract. These volume expansion-contraction cycles lead to alternating stresses in the electrodes which, in turn, causes crack propagation and material fatigue. Cracks emergence at the surface of the electrode and SEI growth exhibit a positive feedback mechanism. The reason is that cracks increase the surface area on which the SEI layer can grow. Electrode cracking can also occur in the interior of the electrodes. This can cause detachment of active material, which can lose electrical contact.
- Lithium plating: Lithium plating denotes the deposition of metallic lithium over the negative electrode's surface. This degradation mechanism takes place specially during charging (specially with high currents) and is promoted at low temperatures. Under such conditions, the potential of the negative electrode can become negative with respective to Li/Li^+, which leads to deposition of lithium onto the surface of graphite particles. This causes loss of lithium inventory and entails possible safety issues. On one hand, plated lithium may react exothermically with the solid-electrolyte interphase and the electrolyte under overcharge conditions. On the other hand, the plated lithium metal can be in the form of dendrites, which may pierce the separator, inducing an internal short circuit. Both scenarios could trigger thermal runaway of the cell.

Structure of the paper. – The structure of this paper continues as follows: firstly, the equivalent-circuit model employed as the base of the comprehensive model is described; then, the SEI degradation model (employed to estimate capacity loss and SEI film resistance) is presented; afterwards, the relative shift between the electrodes' Open Circuit Potential (OCP) curves (which originates a secondary capacity recovery) that takes place as a consequence of the consumption of cyclable lithium in the SEI reaction is described; next, the characterization tests carried out in [37] are summarized and both models (equivalent-circuit and degradation) are coupled to simulate cell operation; the simulation results are then analyzed; finally, the main contributions of this paper are highlighted and possible future research directions are suggested.

MODEL DESCRIPTION. PART 1: EQUIVALENT CIRCUIT

The basis of the proposed model is an equivalent electrical circuit: the ESC model described in [5]. This circuit consists of: an SOC-dependent voltage source, which represents the Open Circuit Voltage (OCV); a hysteresis element; two parallel resistor-capacitor pairs, which represent the dynamic response of the cell due to diffusion processes; and a series resistance, which represents the instantaneous drop in the cell voltage when applying a current. Figure 1 shows the equivalent circuit with black letters representing constant parameters and blue letters representing parameters affected by degradation, in which time dependency has been included.

The Panasonic-cell parameter values were obtained by reproducing the test scripts and estimation method described in [5], applying a current profile corresponding to the Urban Dynamometer Driving Schedule (UDDS) for electric vehicles, as shown in Figure 2. Table 1 collects the nomenclature of the ESC model parameters and their values.

The discrete time equation that describes the cell's response when a current i_{app} is applied is:

$$v[k] = OCV(z[k])\,\big|_k + (M_0 s[k] + Mh[k]) - \left(R_1 i_{R_1}[k] + R_2 i_{R_2}[k]\right) - (R_0 + R_{SEI}[k]) i_{app}[k] \quad (1)$$

where the nomenclature $f(x)\,\big|_k$ symbolizes the dependency of the function or variable f with the variable x at instant k. Overall, Eq. (1) states that cell voltage, v, is the result of adding four terms: an open-circuit voltage term $OCV(z)\,\big|_k$, a hysteresis term $(M_0 s + Mh)$, a diffusion term $-\left(R_1 i_{R_1} + R_2 i_{R_2}\right)$, and an internal resistance term $-(R_0 + R_{SEI}) i_{app}$. The elements of Eq. (1) are calculated as follows:

$$i_{R_j}[k] = exp\left(\frac{-\Delta t}{R_j C_j}\right) i_{R_j}[k-1] + \left(1 - exp\left(\frac{-\Delta t}{R_j C_j}\right)\right) i_{app}[k-1] \quad (2)$$

$$h[k] = A_H[k-1]h[k-1] + (A_H[k-1] - 1)sgn\left(i_{app}[k-1]\right) \quad (3)$$

$$A_H[k] = exp\left(-\left|\frac{\eta_Q[k] i_{app}[k] \gamma \Delta t}{3600 \cdot Q[k]}\right|\right) \quad (4)$$

$$\eta_Q[k] = \begin{cases} 1, & i[k] \geq 0 \quad [discharging] \\ \eta_Q, & i[k] < 0 \quad [charging] \end{cases} \quad (5)$$

$$z[k] = \frac{\theta_n[k] - \theta_n^0[k]}{\theta_n^{100}[k] - \theta_n^0[k]} \quad (6)$$

$$s[k] = \begin{cases} sgn\left(i_{app}[k]\right), & i_{app}[k] \neq 0 \\ s[k-1], & i_{app}[k] = 0 \end{cases} \quad (7)$$

where $j = \{1,2\}$; h is the unitless hysteresis state $-1 \leq h[k] \leq 1$; coulombic efficiency, η_Q, is associated to battery charging only; $\mathrm{sgn}(x)$ is the sign function of x; and θ_n is the negative electrode's stoichiometry ($\mathrm{Li}_{\theta_n}\mathrm{C}_6$), which is calculated in (18). The sampling time Δt must be chosen in accordance to the rate at which the current profile i_{app} varies. In this work, $\Delta t = 60\ s$ has been selected as it is more than sufficient to simulate the cell response to the current profile described below, where current is mostly zero –corresponding to self-discharge tests. Future improved versions of the algorithm may implement adaptive calculation of the time step size, optimizing its value for minimum iterations while keeping the local and the global error low.

Next sections show how (time-varying) cell capacity, Q, and SEI film resistance, R_{SEI}, are calculated employing the degradation model. These two results are incorporated into the ESC equivalent circuit, converting some of the ESC model's constant parameters into time-dependent parameters (blue letters in Figure 1). Capacity variations affect the calculation of the hysteresis coefficient A_H (Eq. (4)) and the definition of the variable z (≡SOC, Eq. (6)) and the OCV curve (Eqs. (1) and (25)), while the resistance of the SEI layer R_{SEI} is added to the initial series resistance R_0, so the total series resistance results $R_0 + R_{SEI}$ (Eq. (1)).

MODEL DESCRIPTION. PART 2: SEI DEGRADATION

The (de)intercalation reaction is the reversible primary reaction that produces energy transfer to (from) the battery. Together with it, unwanted side reactions that degrade the cell also take place. The SEI

reaction is one of the most relevant side reactions in terms of capacity loss. SEI layer growth is caused by the reduction of the organic-solvent component of the electrolyte on the surface of the negative electrode. This side reaction consumes part of the inventory of cyclable lithium causing the cell capacity to decrease and the internal resistance to increase [7].

In this work, degradation is modeled utilizing the zero-dimensional reduced-order model of the SEI reaction proposed by Randall et al. in [18], which is derived from the system of partial differential equations presented by Ramadass et al. in [21]. The SEI layer growth process is modeled for lithium-ion cells with electrolyte containing ethylene carbonate organic solvent, where the solvent reduction reaction is irreversible (Solvent + $2Li^+$ + $2e^-$ ⇔ Products, where multiple different solvent reduction reactions are represented by the average equilibrium potential). Rates of charge and discharge are moderate (the studied range of C-rates is $|i_{app}| \leq 3C$ [18]), and quasi-equilibrium state is assumed, neglecting local variations in electrolyte and solid surface concentration. The effect of mobile electrons and inserted lithium ions on the exchange-current density is considered insignificant. The intercalation and side reactions over the anode are assumed to be uniform, and with anodic and cathodic charge-transfer coefficients $\alpha_a = \alpha_c = 0.5$ [21]. The SEI model is kinetics-limited and applies to post-formation SEI growth.

Two of the starting hypotheses have been reconsidered with respect to [18]:

- The SEI reaction has been considered to occur not only during cell charging, but also during discharging. For example, [38] and [13] confirm that the SEI layer also grows during discharge (although at a slower rate).
- The internal resistance rise coefficient, k_R, has been selected to produce a plausible value of resistance rise at the cell's End Of Life (EOL), instead of calculating it from averaged SEI film properties (density, molecular weight and conductivity), which is difficult and uncertain due to the extreme diversity of components and complex configurations that can appear in the SEI layer [7].

Also, the values of the cell's parameters have been adapted to model the 25 Ah Panasonic NMC cell, instead of the 1.8 Ah Sony 18650 LCO cell originally modeled in [18] to model the 25 Ah Panasonic NMC cell. The majority of the parameters for the Panasonic cell were found using the methods reported in [39], although the remaining parameters were estimated using the values reported in the literature for other cells having graphite NEs. While it is not possible to guarantee that these parameter values are precise for the Panasonic cell, they are assumed as typical values for graphite NEs.

Table 2 collects the nomenclature used in this section.

The set of equations employed to calculate the current density of the SEI side reaction, J_{side} (Eqs. (8) and (17)), is presented next. J_{side} represents the flux of lithium from the SEI layer. Since the sign of J_{side} is always negative, the magnitude of J_{side} represents the rate of lithium loss due to the side reaction that grows the SEI layer. Capacity loss and internal resistance increase are directly related to J_{side} (Eqs. (21) and (22)). At every spatial location in the NE, it is satisfied that $J_{total} = J_I + J_{side}$, where J_{total} and J_I are the total current density and the intercalation current density. Making the simplifying assumption that these are uniform over the thickness of the NE, it is possible to write:

$$J_{total} = J_I + J_{side} = \frac{i_{app}}{Vol_n} \tag{8}$$

Figure 3 shows the directions of J_{total}, J_I and J_{side} under three operation scenarios: cell discharge, idle and charge.

First, the Butler-Volmer Eq. (9) models the reversible (primary) intercalation reaction.

$$J_I = a_n i_{0,n} \left[exp\left(\frac{\alpha_{a,n} F}{R_g T}\eta_n\right) - exp\left(-\frac{\alpha_{c,n} F}{R_g T}\eta_n\right)\right] \tag{9}$$

where the specific area of the electrode, a_n, the exchange current density, $i_{0,n}$, and the intercalation reaction overpotential, η_n, are calculated as follows:

$$a_n = \frac{3\varepsilon_{s,n}}{R_s} \tag{10}$$

$$i_{0,n} = k_n\left((1-\theta_n)c_s^{max}\right)^{\alpha_{a,n}}(\theta_n c_s^{max})^{\alpha_{c,n}} c_e^{\alpha_{a,n}} \tag{11}$$

$$\eta_n = \phi_s - \phi_e - OCP_n - \frac{J_{total}}{a_n} R_{SEI} A_n \tag{12}$$

Considering $\alpha_{a,n} = \alpha_{c,n} = 0.5$ [21] and acknowledging that $\sinh(x) = (e^x - e^{-x})/2$, the next expression is derived from Eq. (9):

$$\eta_n = \frac{2R_g T}{F} asinh\left(\frac{J_I}{2a_n i_{0,n}}\right) \tag{13}$$

The irreversible side reaction is modeled as a function of the SEI reaction overpotential, η_{side}, using the Tafel Eq. (14):

$$J_{side} = -a_n i_{0,side}\, exp\left(-\frac{\alpha_{c,side} F}{R_g T}\eta_{side}\right) \tag{14}$$

$$\eta_{side} = \phi_s - \phi_e - U_{side}^{ref} - \frac{J_{total}}{a_n} R_{SEI} A_n \tag{15}$$

Note that the value of J_{side} is, by definition, always negative (i.e., lithium consumed in the SEI reaction cannot return to be cyclable). Combining Eqs. (12) and (15), η_{side} can be expressed in terms of η_n:

$$\eta_{side} = \eta_n + OCP_n - U_{side}^{ref} \tag{16}$$

Finally, considering $\alpha_{c,side} = 0.5$ [18] and combining (16) with (13), allows to transform Eq. (14) into:

$$J_{side} = -a_n i_{0,side}\, exp\left(-\frac{F\left(OCP_n - U_{side}^{ref}\right)}{2R_g T}\right) exp\left(-asinh\left(\frac{\frac{i_{app}}{Vol_n} - J_{side}}{2a_n i_{0,n}}\right)\right) \tag{17}$$

Here, J_{side} is expressed implicitly but its value can be found algebraically applying the resolution method presented in [33]. Eq. (17) shows that the rate of cyclable lithium loss depends on three variables: the degree of lithiation of the NE, θ_n (since OCP_n and $i_{0,n}$ are functions of θ_n), the applied current, i_{app}, and the temperature, T.

The degree of lithiation of the electrode, θ_{el} (where $el = \{n, p\}$), represents the instantaneous concentration of stored lithium in that electrode with respect to the maximum concentration that the electrode's material can store: $\theta_{el} = c_{s,el}/c_{s,el}^{max}$. In the incremental degradation model, the values of the variables θ_n and θ_p are calculated by counting the input and output flows of lithium ions to/from each electrode, as Eqs. (18) and (19) show:

$$\theta_n[k] = \theta_n[k-1] - \frac{J_l[k]}{\varepsilon_{s,n} F c_{s,n}^{max}} \Delta t \tag{18}$$

$$\theta_p[k] = \theta_p[k-1] + \frac{i_{app}[k]/Vol_p}{\varepsilon_{s,p} F c_{s,p}^{max}} \Delta t \tag{19}$$

Incremental SEI layer thickness growth, $\Delta\delta_{SEI}$ (in m), capacity loss, ΔQ_{side}^{loss} (in Ah), and resistance increase, ΔR_{SEI} (in Ω), caused by growth of the SEI layer can be estimated from the current density J_{side}:

$$\Delta\delta_{SEI}[k] = -\frac{M_P}{a_n \rho_P F} \Delta t J_{side}[k] \tag{20}$$

$$\Delta Q_{side}^{loss}[k] = -\frac{Vol_n}{3600} \Delta t \, J_{side}[k] \tag{21}$$

$$\Delta R_{SEI}[k] = -k_R \Delta t \, J_{side}[k] \tag{22}$$

where M_P and ρ_P are the average molecular weight and density of the SEI layer components, and k_R is the (positive) coefficient of SEI layer resistance increase. Note that SEI layer thickness growth, $\Delta\delta_{SEI}$, capacity loss, ΔQ_{side}^{loss}, and film resistance variation, ΔR_{SEI}, are all positive because the value of J_{side} is always negative. Eq. (1) of the ESC model is updated with (22) and Eq. (4) is updated with (21). The NE's degree of lithiation $\theta_n[k]$ and lithiation boundaries $\{\theta_n^0[k], \theta_n^{100}[k]\}$ (Eq. (6)) are also affected by ΔQ_{side}^{loss}, as explained in the next section.

Finally, since independent estimates of $i_{0,side}$ and U_{side}^{ref} are not available, the lumped parameter k_{SEI} has been defined to group both:

$$k_{SEI} = a_n i_{0,side} \, exp\left(F \frac{U_{side}^{ref}}{2R_g T}\right) \tag{23}$$

With this, Eq. (17) particularized at discrete time k results in:

$$J_{side}[k] = -k_{SEI} \, exp\left(-\frac{F \, OCP_n(\theta_n[k], T)}{2R_g T}\right) exp\left(-asinh\left(\frac{\frac{i_{app}[k]}{Vol_n} - J_{side}[k]}{2a_n i_{0,n}(\theta_n[k])}\right)\right) \tag{24}$$

The estimation of the parameters k_R and k_{SEI} for the case of constant temperature $T = 25\,°C$ is explained below. Table 3 collects the values of the rest of the parameters used in the formulation of the model. Some values were measured in the study of the Panasonic cell [39], others have been estimated from literature review [21, 40–46] and the rest of them have been estimated based on cell measurements.

The initial electrodes' lithiation boundaries of the Panasonic cell, $\{\theta_p^0[0], \theta_p^{100}[0], \theta_n^0[0], \theta_n^{100}[0]\}$, have been found based on data obtained from characterization tests of the electrodes' OCP [39] and of the initial cell's OCV [37]. The extreme degrees of lithiation are calculated by fitting the difference $OCP_p(\theta_p)$ minus $OCP_n(\theta_n)$, to the initial OCV curve $OCV(z)\,|_0$ referring the variables θ_p, θ_n and z to a common reference [47]. The volume fraction of solid in the NE, $\varepsilon_{s,n}$, is calculated to be consistent with the rest of the cell parameters: $\varepsilon_{s,n} = \frac{3600 \cdot Q[0]}{Vol_n c_{s,n}^{max} F(\theta_n^{100}[0] - \theta_n^0[0])}$ (see Eq. (36)). Microscopical images of the NE in [39] validate the value obtained for $\varepsilon_{s,n}$.

The model presented in this work considers constant temperature $T = 25\,°C$. However, different operation temperatures could easily be considered by coordinately using several T-dependent models developed for a number of T values (to account for the dependence on temperature of the ESC parameters, the OCP_p, OCP_n and OCV curves, and k_{SEI}), and interpolating for intermediate temperature values.

MODEL DESCRIPTION. PART 3: SECONDARY CAPACITY RECOVERY

This section describes how the capacity loss due to the SEI reaction modifies the curve $OCV(z)\,|_k$ and how this, in turn, modifies the NE's minimum (θ_n^0) and maximum (θ_n^{100}) lithiation boundaries. A small extension to the range of allowed degrees of lithiation ($\theta_n^{100} - \theta_n^0$) takes place and, therefore, a fraction of the capacity lost in the SEI reaction, $Q_{side}^{loss}[k] = \sum_k \Delta Q_{side}^{loss}[k]$, is recovered in this process [48, 49]. This process is a consequence of the displacement of the OCP curves due to cell aging described in [12, 50].

Relationship between the curves OCP_p, OCP_n and OCV. – Figure 4 provides an intuitive representation of the variables θ_p and θ_n as lithiation levels. Bold letters and the green horizontal line represent the cell's state at a given instant k. Regular letters indicate other known states in the three represented axes: θ_p (blue), θ_n (orange) and z (green).

Note that not all θ_p and θ_n values are allowed. Practical cells do not use the electrodes' entire capacity in order to stay away from boundaries which would lead either to rapid cell degradation or to power depletion [5]. Therefore, lithium cycling is practically restricted to a limited range: $0 < \theta_p^{100} \leq \theta_p \leq \theta_p^0 < 1$ and $0 < \theta_n^0 \leq \theta_n \leq \theta_n^{100} < 1$, where θ_p^0 and θ_n^0 are the degrees of lithiation of the positive electrode and the negative electrode when the cell is at $z = 0\%$ (defined for this cell by $OCV = V_{min} = 2.1\,V$), and θ_p^{100} and θ_n^{100} are the degrees of lithiation of PE and NE when the cell is at $z = 100\%$ (defined for this cell by $OCV = V_{max} = 4.1\,V$). Note that the cell's capacity is consequently proportional to the extent of the range ($\theta_n^{100} - \theta_n^0$), as indicated by the double-arrowed black line in Figure 4.

The electrodes' lithiation boundaries $\{\theta_p^0, \theta_p^{100}, \theta_n^0, \theta_n^{100}\}$ are not fixed but vary with degradation. The relationship between three curves: OCP_p, OCP_n, and OCV, must be studied to find the values of the electrodes' lithiation boundaries at any instant k $\{\theta_p^0[k], \theta_p^{100}[k], \theta_n^0[k], \theta_n^{100}[k]\}$ as the cell ages. This enables calculation of the remaining cell capacity $Q[k]$ as explained below.

The curve OCV is calculated as the difference between OCP_p and OCP_n (see Eq. (25)). Since these three curves depend on different variables, $OCV(z)\,|_k$, $OCP_p(\theta_p)$ and $OCP_n(\theta_n)$, a common reference must be selected to study how they interrelate. In this work, the NE's degree of lithiation θ_n has been selected as the reference.

$$OCV\big(z(\theta_n)\,|_k\big)\,|_k = OCP_p\big(\theta_p(\theta_n)\,|_k\big) - OCP_n(\theta_n) \tag{25}$$

The curves $OCP_p(\theta_p)$ and $OCP_n(\theta_n)$ remain valid throughout the whole cell's lifespan, while the function $OCV(z)\,|_k$, as well as the relationships $\theta_p(\theta_n)\,|_k$ and $z(\theta_n)\,|_k$ vary over time, as explained below. The nomenclature "$|_k$" represents this fact: $f(\theta_n)\,|_k$ symbolizes the dependency of the function or variable f with the variable θ_n (the common reference) at the instant k. Prior to studying how $OCV(z|_k)\,|_k$ varies with degradation, the initial conditions ($k = 0$) are examined next.

Study of initial lithiation boundaries. – The initial electrodes' lithiation boundaries, $\{\theta_p^0[0], \theta_p^{100}[0], \theta_n^0[0], \theta_n^{100}[0]\}$, have been found for the Panasonic cell based on data from the characterization tests of the electrodes' OCP and on the cell's OCV curve of the fresh cell performed in [39]. The lithiation boundaries are calculated by fitting the difference OCP_p minus OCP_n to the measured OCV curve utilizing the Matlab function *fminsearch*. The best fit yields an RMS voltage error of 17.7 mV, as shown in Figure 5.

The initial electrodes' lithiation boundaries are calculated by minimizing the error between the curve resulting from the subtraction $OCP_p\big(\theta_p(\theta_n)\,|_0\big) - OCP_n(\theta_n)$ and the measured curve $OCV\big(z(\theta_n)\,|_0\big)\,|_0$, being the range of $\theta_n \in \left[\theta_n^0[0], \theta_n^{100}[0]\right]$ and $\theta_p \in \left[\theta_p^0[0], \theta_p^{100}[0]\right]$ the variables to optimize. The fit is best when the appropriate ranges θ_n and θ_p are considered. This fitting yields the values of the initial lithiation boundaries provided in Table 3. These values delimit the initial relative position between the PE's and the NE's stoichiometry windows.

Displacement of the OCP curves. – The lithium loss caused by the SEI reaction produces a relative displacement between the OCP curves: the NE's degree of lithiation θ_n corresponding to a given PE's degree of lithiation θ_p decreases as the SEI layer consumes cyclable lithium [12]. The displacement of the θ_n axis between Figure 6.A and Figure 6.B$_1$ or in Figure 7 exemplify this process. Figure 6 and Figure 7 are two graphical representations that complement each other, as both show different aspects of the degradation process of a cell over a prolonged self-discharge period. Figure 6 illustrates the relative displacement between the PE's and the NE's stoichiometric windows produced by the SEI reaction, while Figure 7 represents the corresponding displacement between the OCP curves of both electrodes and the consequent recalculation of the electrodes' lithiation boundaries and of the OCV curve. Variables θ_p and θ_n represented in Figure 7 do not cover their whole ranges (which, by definition, are [0,1]) but only the ranges identified in [39]. Figure 6 is a conceptual illustration while Figure 7 corresponds to the studied cell.

Figure 6.A represents the state of a fully charged cell (instant k_A). Figure 6.B_1 represents that cell after a prolonged self-discharge time (instant k_B). Figure 6.B_2 and Figure 6.B_3 show how $\{\theta_p^0, \theta_p^{100}, \theta_n^0, \theta_n^{100}\}$ change as the cell ages. Although in practice the new electrodes' lithiation boundaries are unknown until fully discharging and recharging the cell, it is possible to compute them theoretically already as in the cell's state B_1. Figure 6.B_2 and Figure 6.B_3 represent the thought experiment of fully discharging (B_2) and recharging (B_3) the cell that would lead to experimentally finding the updated electrodes' lithiation boundaries at k_B. There is no capacity variation in B_2 and B_3 since they are a thought experiment.

In this illustration, a large capacity loss $Q_{side}^{loss}\big|_A^B = \sum_{k_A}^{k_B} \Delta Q_{side}^{loss}[k]$ occurs between the initial stage (A) and the degraded stage (B). Eqs. (8), (17) and (18), show that the NE loses Li due to the SEI side reaction. Thus, θ_n decreases by an amount $\theta_n^{loss}\big|_A^B = \sum_{k_A}^{k_B} \Delta\theta_n^{loss}[k]$. Meanwhile, the PE's degree of lithiation (θ_p) remains the same according to Eqs. (8) and (19), since the cell is unloaded during self-discharge. To be consistent with the NE's extra loss of lithium, its stoichiometry window needs to be shifted by an offset $\theta_n^{loss}\big|_A^B$ with respect to the PE's stoichiometry window (θ_n axis moves up in Figure 6.B_1). The relative displacement $\Delta\theta_n^{loss}$ can be quantified from:

$$\Delta\theta_n^{loss}[k] = \frac{3600}{\varepsilon_{s,n} Vol_n c_{s,n}^{max} F} \Delta Q_{side}^{loss}[k] \tag{26}$$

Taking θ_n as the common axis (i.e. the fixed axis), $\theta_p(\theta_n)\big|_k$ and, together with it, $OCP_p\big(\theta_p(\theta_n)\big|_k\big)$, undergo a relative displacement [12] (see Figure 7). That is, the translation in Eq. (27) –the derivation of these expressions is included in the Appendix at the end:

$$\theta_p(\theta_n)\big|_k = \theta_p^0[k] - \frac{\theta_p^0[k] - \theta_p^{100}[k]}{\theta_n^{100}[k] - \theta_n^0[k]}(\theta_n - \theta_n^0[k]) = \theta_p\big(\theta_n + \Delta\theta_n^{loss}[k]\big)\big|_{k-1} \tag{27}$$

The OCV curve is updated by combining this result with Eq. (25):

$$OCV\big(z(\theta_n)\big|_k\big)\big|_k = OCP_p\big(\theta_p\big(\theta_n + \Delta\theta_n^{loss}[k]\big)\big|_{k-1}\big) - OCP_n(\theta_n) \tag{28}$$

The model uses Eq. (28) instead of the measured OCV curve (at the initial moment, the green curve in Figure 5 is used instead the black dotted curve). This introduces some voltage error but allows to account for OCV recalculation due to degradation. The result of Eq. (28) is used to generate a look-up table that links OCV directly to θ_n at any instant k. The domain of the function $OCV(z)\big|_k$ is $z \in [0,1]$ or, equivalently, the domain of $OCV\big(z(\theta_n)\big|_k\big)\big|_k$ is $\theta_n \in \big[\theta_n^0[k], \theta_n^{100}[k]\big]$. Boundary values of θ_n are defined by V_{min} and V_{max}, and are calculated by inversely using the look-up table generated from (28):

$$V_{min} = OCV\big(z(\theta_n^0[k])\big|_k\big)\big|_k \Leftrightarrow \theta_n^0[k] = z^{-1}\big(OCV^{-1}(V_{min})\big|_k\big)\big|_k \tag{29}$$

$$V_{max} = OCV\big(z(\theta_n^{100}[k])\big|_k\big)\big|_k \Leftrightarrow \theta_n^{100}[k] = z^{-1}\big(OCV^{-1}(V_{max})\big|_k\big)\big|_k \tag{30}$$

The Matlab function *interp1* has been employed to calculate the updated lithiation boundaries of the NE:

- *theta0n(k) = interp1(OCVvalidrange, validThrange, Vmin)*
- *theta100n(k) = interp1(OCVvalidrange, validThrange, Vmax)*

where *OCVvalidrange* is the result of $OCP_p - OCP_n$ in the region where both curves are defined; and *validThrange* is the corresponding region of θ_n values (remind that θ_n has been chosen as the common reference in this work) in which OCP_p and OCP_n coexist after the relative displacement caused by the loss of cyclable lithium in the SEI reaction. Eqs. (1) and (6) of the ESC model described above are updated with the updated curve $OCV\left(z(\theta_n)\,\middle|_{\,k}\right)\middle|_{\,k}$ and the recalculated values of $\theta_n^0[k]$ and $\theta_n^{100}[k]$.

Secondary capacity recovery. – Following SEI degradation, one might expect to have a remaining capacity equal to $Q[k-1] - \Delta Q_{side}^{loss}[k]$, but this is not the case. The definition of $z = 0$ and $z = 1$ based on open-circuit voltage levels leads to a small capacity recovery. After the displacement between the curves OCP_p and OCP_n (instant k_B in Figure 6 and Figure 7), $OCV[k_B]$ is lower than V_{max} (see the green cross in Figure 7). Therefore, the cell SOC at this point is no longer 100% but lower. The reason is that V_{max} does not correspond to $\left(\theta_n^{100}[k_A] - \theta_n^{loss}\,\middle|_{\,A}^{\,B}\right)$ and, similarly, V_{min} does not correspond to $\theta_n^0[k_A]$.

Fine-tuning of the electrodes' lithiation boundaries is necessary. Specifically, $\theta_n^0[k]$ as calculated in (29) results in a value smaller than $\theta_n^0[k-1]$ and $\theta_n^{100}[k]$ as calculated in (30) results in a value greater than $\left(\theta_n^{100}[k-1] - \Delta\theta_n^{loss}[k]\right)$. Incremental θ_n^0 adjustment is denoted $\Delta\theta_n^{0,tune}$, and θ_n^{100} adjustment is denoted $\Delta\theta_n^{100,tune}$:

$$\Delta\theta_n^{0,tune}[k] = \theta_n^0[k] - \theta_n^0[k-1] \tag{31}$$

$$\Delta\theta_n^{100,tune}[k] = \theta_n^{100}[k] - \left(\theta_n^{100}[k-1] - \Delta\theta_n^{loss}[k]\right) \tag{32}$$

(Note that $\theta_n^{0,tune}[k] = \sum_k \Delta\theta_n^{0,tune}[k] < 0$ and $0 < \theta_n^{100,tune}[k] = \sum_k \Delta\theta_n^{100,tune}[k] < \theta_n^{loss}$ for all k because both curves $OCP_p\left(\theta_p\right)$ and $OCP_n(\theta_n)$ are monotonically decreasing.)

This process extends the range of allowed degrees of lithiation causing a small secondary capacity recovery, $\left(\Delta Q_{\theta_0}^{gain} + \Delta Q_{\theta_{100}}^{gain}\right)$:

$$\Delta Q_{\theta_0}^{gain}[k] = \frac{\varepsilon_{s,n} Vol_n c_{s,n}^{max} F}{3600}\left(-\Delta\theta_n^{0,tune}[k]\right) \tag{33}$$

$$\Delta Q_{\theta_{100}}^{gain}[k] = \frac{\varepsilon_{s,n} Vol_n c_{s,n}^{max} F}{3600}\Delta\theta_n^{100,tune}[k] \tag{34}$$

Adding the three contributions ΔQ_{side}^{loss}, $\Delta Q_{\theta_0}^{gain}$ and $\Delta Q_{\theta_{100}}^{gain}$ results in a net capacity loss ΔQ_{tot}^{loss}. Figure 8 contains several zooms of Figure 7 that illustrate the post-degradation recalculation of the electrodes' lithiation boundaries. Figure 8 reveals that $\theta_n^{0,tune}$ is almost insignificant and, thus, so is $Q_{\theta_0}^{gain}$ too,

while $\theta_n^{100,tune}$ accounts for nearly all the NE's stoichiometric window extension and, consistently, $Q_{\theta_{100}}^{gain}$ accounts for nearly all the capacity recovery.

$$\Delta Q_{tot}^{loss}[k] = \Delta Q_{side}^{loss}[k] - \left(\Delta Q_{\theta_0}^{gain}[k] + \Delta Q_{\theta_{100}}^{gain}[k]\right) \tag{35}$$

$$Q[k] = Q[k-1] - \Delta Q_{tot}^{loss}[k] = \frac{\varepsilon_{s,n} Vol_n c_{s,n}^{max} F}{3600}(\theta_n^{100}[k] - \theta_n^0[k]) \tag{36}$$

The model output is $Q[k]$, which relates to SOH straightforwardly:

$$SOH[k] = Q[k]/Q[0] \tag{37}$$

Continuing with the example of degradation over a prolonged self-discharge period illustrated in Figure 6 and Figure 7, the recalculation of $\theta_n^0[k_B]$ and $\theta_n^{100}[k_B]$ based on the abovementioned voltage criteria is illustrated in Figure 8.a.2) and Figure 8.b.2). Correspondingly, a fraction of the capacity lost is recovered, associated to recalculation of the electrodes' lithiation boundaries: $Q_{\theta_0}^{gain}\big|_A^B = \sum_{k_A}^{k_B} \Delta Q_{\theta_0}^{gain}[k]$ and $Q_{\theta_{100}}^{gain}\big|_A^B = \sum_{k_A}^{k_B} \Delta Q_{\theta_{100}}^{gain}[k]$ are shown in Figure 6.B$_2$ and Figure 6.B$_3$. The secondary capacity recovery is caused by the incorporation of lithium from the NE's and the PE's previously unused lithium reserves into the cyclable lithium range.

Figure 9 shows the ratio of capacity recovery, $\left(Q_{\theta_0}^{gain}[k] + Q_{\theta_{100}}^{gain}[k]\right) = \sum_k \left(\Delta Q_{\theta_0}^{gain}[k] + \Delta Q_{\theta_{100}}^{gain}[k]\right)$, to the capacity loss caused by the SEI reaction $Q_{side}^{loss}[k] = \sum_k \Delta Q_{side}^{loss}[k]$ as cell degradation progresses. The range represented on the x axis corresponds to the whole lifespan of the cell, considering that its EOL corresponds to a 20% total capacity loss: $Q[k_{EOL}] = 0.8 \cdot Q[0] \Leftrightarrow Q_{tot}^{loss}[k_{EOL}] = 0.2 \cdot Q[0]$ –typical EOL definition for electric vehicles. It is worth mentioning that batteries can get a second life after surpassing this conventional EOL criterion: they can then be used in less demanding applications in terms of energy density and power density, such as storage elements in renewable energy systems. Several look-up tables, apart from the initial cell characterization look-up tables, $OCV(z)\big|_0$, $OCP_p(\theta_p)$ and $OCP_n(\theta_n)$ have been created to simplify and accelerate calculations, specifically:

- $OCV\left(z(\theta_n)\big|_k\right)\big|_k$
- $J_{side}(i_{app}, OCP_n, T)$
- $\theta_n^0(\Delta\theta_n^{loss})$ and $\theta_n^{100}(\Delta\theta_n^{loss})$
- $\Delta Q_{\theta_0}^{gain}(\Delta\theta_n^{0,tune})$ and $\Delta Q_{\theta_{100}}^{gain}(\Delta\theta_n^{100,tune})$

Creating look-up tables for the intermediate variables ΔQ_{side}^{loss}, $\Delta\theta_n^{loss}$, $\Delta\theta_n^{0,tune}$ and $\Delta\theta_n^{100,tune}$ has been discarded because their calculation only involves one basic mathematical operation (multiplication or subtraction) each: see Eqs. (21), (26), (31) and (32).

The SOC-estimation method employed (see Eq. (6)) is known as the electrochemical method [51]. Two enhancements have been introduced over the coulomb counting method: first, the proposed model does not only account for the main reaction (intercalation), but also considers lithium flux due to the SEI side reaction (see Eqs. (8) and (18)); and second, the model accounts for the secondary capacity recovery process, by fine-tuning the electrodes' lithiation boundaries (variable $\theta_n^0[k]$ and $\theta_n^{100}[k]$), as explained above.

EXPERIMENTAL

The authors are not aware of any other papers that combine an equivalent-circuit model (or other simplified model) of cell dynamics with a reduced-order model of SEI-layer growth against which to compare the results to validate the model. However, Figure 2 shows that cell voltage versus time for a sequence of UDDS profiles is well-matched by the ESC model. Further, the reduced-order SEI model of [18] was shown in simulation to match the full-order model with an error lower than 0.45% in the range $10\% \leq$ SOC $\leq 90\%$. On the basis of the good performance that both models demonstrate separately, the performance of the comprehensive model (which results from coupling them) is evaluated next by comparing its predictions with the actual cell response, considering the current profile utilized in [37].

Nine Panasonic cells were tested in [37] to characterize the degradation process over long periods of self-discharge. The following tests were performed:

- OCV Tests (OCVT): Two accurate estimates of cell capacity, at the beginning and at the end of the sequence of tests.
- Self-Discharge Tests (SDT): Three two-month-each self-discharge tests. Different cells were tested at different temperatures: 0 °C, 25 °C and 50 °C.
- Pulse Tests (PT): One before and one after each SDT (four PTs), to estimate internal resistance. Each PT estimates the internal resistance at four SOC levels: SOC = {20%, 40%, 60%, 80%} subjecting the cell to $20\ ms$, $30\ A$ pulses.
- Capacity Single Loops (CSL): Two fast capacity estimates, after PT2 and after PT3.

The complete sequence of tests carried out was: $OCVT_1$→ PT_1 → SDT_1 → PT_2 → CSL_1 → SDT_2 → PT_3 → CSL_2 → SDT_3 → PT_4 →$OCVT_2$.

Initial internal resistance, $R_0 = 1.3164\ m\Omega$, is the result of averaging the initial internal resistance measured at four SOC levels (SOC $= \{20\%, 40\%, 60\%, 80\%\}$) in PT_1, as described in [37]. The results of the subsequent Pulse Tests have been discarded to estimate k_R because they did not show a monotonically increasing trend as would be expected from (22). A plausible explanation for this phenomenon is that the (rather rigid) SEI layer may have cracked due to expansions and contractions experienced by the NE during cell charging and discharging [13]. When the SEI layer cracks, a new path of higher conductivity opens (along with an additional SEI formation point) [52]. This effect, however, has minor importance in the overall resistance increase tendency [53–55]. The parameter k_R has been calculated assuming that the internal resistance at the cell's EOL doubles the initial($R[k_{EOL}] = 2R_0$). The obtained value is: $k_R = 5.5827 \cdot 10^{-12}\ \Omega\ m^3\ A^{-1}\ s^{-1}$.

The capacity loss between $OCVT_1$ and $OCVT_2$, $Q\left[k_{OCVT_1}\right] = 24.863\ Ah$ and $Q\left[k_{OCVT_2}\right] = 24.260\ Ah$, has been used in this work to calculate the parameter k_{SEI} of the degradation model at 25 °C. Capacity was calculated by integrating the discharge current, measured by a high precision current sensor (0.02% accuracy). A "pulsed CC/CV-like" discharge process was applied, as described in [37].

Unfortunately, the results of OCVTs and CSLs are not comparable with each other because different test procedures were used, so the CSL capacity estimations have been discarded given their lower precision. The parameter k_{SEI} has been calculated iteratively as the value that produces a capacity loss in simulation equal to the real one. The obtained value is: $k_{SEI} = 1.2327 \cdot 10^{-3} A\ m^{-3}$.

RESULTS

Cell response to a load profile coincident with the set of tests performed between the initial and the final capacity estimates (i.e. PT_1 → SDT_1 → PT_2 → CSL_1 → SDT_2 → PT_3 → CSL_2 → SDT_3 → PT_4 →$OCVT_2$) has been simulated using the ESC equivalent-circuit cell model complemented with the degradation model presented above. The temperature considered for the simulation is $T = 25\ °C$. Blue and red curves in Figure 10 are the simulation results., while yellow curves are the actual values of the variables logged during testing.

- Figure 10.a represents the simulated cell capacity Q_{sim} (blue) and the evolution of the simulated state of charge SOC_{sim} (red). The capacity loss in simulation coincides with the real value Q_{real} (yellow circles) in that points where the latter is available. This was expected given that k_{SEI} has been estimated precisely to fit this result. Note that the actual capacity is only known at the beginning and at the end of the test; the yellow dashed line only connects both points, but the actual path between them is unknown.
- Figure 10.b shows the applied current i_{app} (yellow) and the current associated to cyclable lithium loss $i_{side} = J_{side} Vol_n$ (blue). Coherently with Randall's model, J_{side} is high when so too are the charge current and the cell SOC (or, equivalently, θ_n). Also, the self-limiting characteristic of the SEI side reaction is captured by the model –note that (the absolute value of) J_{side} gradually decreases along the self-discharge periods, and that both ΔQ_{side}^{loss} and ΔR_{SEI} are proportional to J_{side}.
- Figure 10.c represents the cell's internal resistance increase. The SEI film resistance rises at a rate determined by the parameter k_R estimated above. The simulation prediction differs from the resistance measured in the PTs in [37] (brown, yellow, purple and green curves) because the measured resistance abnormally deviates from the expected increasing trend. SEI-layer cracking has been suggested above as a possible explanation for the (temporary) reduction of the cell's resistance. However, this effect has been proven to be minor since resistance is expected to grow in the long term [53–55].
- Figure 10.d shows the evolution of the open circuit voltage OCV_{sim} (red), the simulated cell voltage v_{sim} (blue), and the measured cell voltage v_{real} (yellow). OCV_{sim} and v_{sim} are almost undistinguishable because current is either zero or very low during the whole set of tests, so diffusion voltage $-\left(R_1 i_{R_1}[k] + R_2 i_{R_2}[k]\right)$ and instantaneous voltage drop $-(R_0 + R_{SEI}[k]) i_{app}[k]$ are consequently small, while hysteresis voltage ($M_0 s[k] + Mh[k]$) is typically small too in NMC batteries. The RMS error between v_{sim} and v_{real} is $28.7\ mV$.

- Figure 10.d.zoomSDT$_2$ shows that the cell's voltage decreases over self-discharge because of the relative shift between the NE's and the PE's stoichiometric windows (see Figure 6.B$_1$ or green cross in Figure 7). This is, indeed, qualitatively predicted by the model although, quantitatively, the model predicts a voltage drop smaller than the one observed in the experimental test.
- Figure 10.d.zoomCSL$_2$ show that the agreement between v_{sim} and v_{real} is good (although not perfect) except for low values of the OCV vs. SOC curve, under operation scenarios with non-zero current, such as cell charge and discharge. The voltage curve predicted by the model replicates the shape of v_{real} but seems to be out of phase.

DISCUSSION

Overall, the simulation results show good performance predicting capacity loss and voltage response under the simulated scenario. On one hand, since the model parameter k_{SEI} has been estimated by adjusting the simulated capacity loss to the actual capacity lost between OCVT$_1$ and OCVT$_2$, it is evidently satisfied that Q_{sim} coincides with Q_{real} at the points when the latter is known. On the other hand, the ESC parameters were estimated in tests dissimilar to SDTs, in which a much faster current profile (the UDDS, for electric vehicles, which represents city driving conditions) was used to characterize the cells –see Figure 2. Therefore, the good agreement between v_{sim} and v_{real} exhibited in Figure 10.d was not trivially expected. On the contrary, such agreement is noteworthy as it validates the performance of the model. Note that the model's RMS voltage error, $28.7\ mV$, is similar to that reported by state-of-the-art reduced-order physics-based models.

The voltage differences observed in Figure 10 zooms are topics of future research. On one hand, the voltage error observed in Figure 10.d.zoomCSL$_2$ is most likely due to insignificant inaccuracies in the employed electrodes' OCP curves $OCP_p(\theta_p)$ and $OCP_n(\theta_n)$ and/or the initial OCV curve $OCV(z)\big|_0$ or to wrong estimation of the initial lithiation boundaries. On the other hand, the voltage drop over self-discharge degradation in Figure 10.d.zoomSDT$_2$ is not fully captured by the proposed model, and capacity decay seems rather linear (which is the case in long-term degradation [56], but fails to show the expected square-root-of-time initial tendency [57]); there are three plausible causes to explain these issues:

- Hypothesis #1. The calculation of the initial lithiation boundaries of the negative electrode might be inaccurate:

J_{side} mainly depends on the current rate and on the open circuit potential of the negative electrode, $OCP_n(\theta_n)$ –apart from temperature, which does not change in the studied case. Thus, wrong initialization of $\theta_n[0]$ could have led to imprecise J_{side} estimations.

The voltage fit performed (by minimizing voltage error between the measured initial OCV curve and OPC_p minus OCP_n, see Eq. (25) with $k = 0$) might have yielded inexact initial negative electrode's lithiation boundaries, $\{\theta_n^0[0], \theta_n^{100}[0]\}$. This, in turn, may arise from the fact that the measured curves

$OCP_p(\theta_p)$ and $OCP_n(\theta_n)$ [39] do not cover the whole lithiation range of the electrodes $\theta_p, \theta_n \in [0,1]$ but a smaller range, as shown in the x-axes of Figure 7.

The initial degree of lithiation of the NE, $\theta_n[0] = \theta_n^{100}[0] = 0.5262$, results in a plateau of the curve $J_{side}(i_{app}, \theta_n, T = 25\,°C)$ for any value of i_{app}, as shown in Figure 11. This locally produces linear capacity decay, as J_{side} is almost constant for immediately lower θ_n values. Since a reduction of θ_n does not significantly modify J_{side}, the tendencies of δ_{SEI}, Q_{side}^{loss} and R_{SEI} result rather linear locally – recall that δ_{SEI}, Q_{side}^{loss}, and R_{SEI} are proportional to the integral of J_{side}. A higher value of $\theta_n^{100}[0]$ (which is probably more accurate, as suggested in [47]) would produce faster decline of J_{side} as θ_n decreases, because $\mathrm{d}J_{side}/\mathrm{d}\theta_n$ is steeper in that region of the J_{side} curves.

The error between the measured and the calculated initial OCV vs. SOC curve (Figure 5) translates to the simulation results. This explains approximately $17.7\,mV$ RMS voltage error over the CSL tests (Figure 10.d.zoomCSL_2). However, there is more to it, as the predicted and measured voltage curves in Figure 10.d.zoomCSL_2 are out of phase. This most likely results from the cell being extra discharged compared to the model prediction. This suggest an additional reversible mechanism, which can also explain the voltage drop during SDTs. This is Hypothesis #3 –see below.

- Hypothesis #2. The fitting strategy used to estimate k_{SEI} or the proposed model might be insufficiently accurate:

If this was the case, the performance of the proposed combination of equivalent-circuit model with reduced-order physics-based model might be improved employing more precise SEI models. Such models should be simplified to reduce their computational complexity, so that they can be implemented on a BMS. Two options are suggested: the SEI growth model of Fu–Fergus et al. [58], or the model of Safari et al. [32] in one of its reduced-order forms [34].

- Hypothesis #3. There are other processes apart from SEI growth having influence on cell voltage during self-discharge:

The last hypothesis assumes that the problem might arise not from the model itself but from more basics assumptions. If this was the case, the proposed model might be correct but incomplete, so it should be complemented by modeling other mechanism(s) capable of producing voltage drop in an unloaded cell –see Figure 10.d.zoomSDT_2. Thus, SEI layer growth would not be the dominant mechanism determining cell voltage during self-discharge, but other reversible process instead –at least at high SOC. Actually, it does not seem feasible that the voltage drop in Figure 10.d.zoomSDT_2 was totally caused by loss of lithium inventory. Indeed, the capacity loss associated to $20\,mV$ voltage drop (over two months) would be much higher than the observed value if it was exclusively caused by irreversible processes. Note that, according to the proposed model, Q_{tot}^{loss} associated to a $20\,mV$ voltage drop would be greater than $10\%\,Q[0]$ while the actual capacity loss over the whole test period (which involves three such SDTs) is only $2\%\,Q[0]$. Thus, the fact is the cells did not lose that much capacity permanently, so there seems to exist a second mechanism driving voltage down during self-discharge. Such mechanism would cause loss of charge without causing loss of lithium inventory, since the process does not cause degradation (it is a reversible process). Considering all the reasoning above, self-discharge caused by a small-magnitude electrochemical internal short circuit [59] is an obvious

candidate to explain the observed voltage drop. Developing a model for this mechanism and combining it with the SEI growth could yield valuable results to verify this hypothesis.

CONCLUSIONS

This paper proposes a degradation model of Li-ion cells with graphite negative electrodes that harmonizes the simplicity of the equivalent-circuit model from [5] with the prediction of capacity loss and internal resistance increase due to SEI degradation provided by the model presented in [18, 21]. A single degradation mechanism has been modeled, specifically, SEI layer growth, one of the main causes of capacity loss. The proposed discrete model computes the shrinkage of the NE's stoichiometric window (which is proportional to the remaining capacity) caused by loss of cyclable lithium consumed in the SEI side reaction.

Defining SOC = 100% and SOC = 0% by voltage levels V_{max} and V_{min} leads to recovering a fraction of that capacity loss (roughly between 11% and 17.5%, see Figure 9) because part of the previously unused lithium reserve from both electrodes starts to be cycled. This secondary capacity recovery process has been quantified by modeling the displacement of the electrode's OCP curves caused by the loss of cyclable lithium, the recalculation of the OCV curve, and the resulting recalibration of the NE's stoichiometric window.

Simulation results produced by the proposed model have been compared to measured cell response in experimental testing showing overall good performance (see Figure 10). Nevertheless, it would be interesting to further validate the model with a different testing set-up and to investigate the causes of voltage drop disagreement over self-discharge periods. Also, different SEI models could be applied to evaluate if performance is improved.

The proposed model can be used to perform predictive control of batteries oriented toward extending their lifetime. With this aim, precomputing the degradation caused by a set of variables combinations (current, SOC and temperature) representative of realistic operation conditions, and creating look-up tables from these results, help to further simplify the calculations.

The presented model is a promising first step towards the creation of simple battery models suitable for BMS controls by coupling equivalent-circuit models with reduced-order physics-based models of the principal degradation mechanisms.

Suggested future works. – The presented model has risen a number of questions that may inspire new research works. They are listed next:

- The model allows to estimate battery's SOC and SOH under any applied current profile. Thus, it could be employed to economically optimize the operation of a microgrid, considering the amortization of the battery energy storage system. The model predicts how possible control actions would affect the battery in terms of capacity loss, which allows to evaluate the amortization of the battery, including this term in the cost function of the optimization problem to determine the best possible current profile.

- The proposed model demonstrates fast calculations in Matlab in a desktop computer but the code has not been adapted to program a BMS microcontroller. This could be done to test its performance in real time applications.
- The present kinetics-limited model of SEI growth could be complemented with a diffusion-limited model.
- The degradation model could also be complemented by including additional degradation mechanisms, such as lithium plating.
- The fixed-step algorithm could be improved with a variable step size that adaptively calculates the time step size, optimizing its value for minimum iterations while keeping the error low.
- The comparison of the simulation results with the measured voltage shows that voltage drop not explained by the model occurs in reality. An additional reversible mechanism, such as self-discharge through an electrochemical internal short circuit is likely to be behind the observed voltage mismatch.

ACKNOWLEDGMENTS

This article has been possible with the support of the Spanish Ministerio de Ciencia, Innovación y Universidades (MICINN) and the European Social Fund (ESF): BES-2016-077460 and the grants DPI2015-67292-R and DPI2017-84572-C2-1-R.

APPENDIX

Equations governing stoichiometric windows displacement – The equations involved in the derivation of Eq. (27), which contains two equivalent expressions, are separately reviewed next: $\theta_p(\theta_n)\big|_k = \theta_p^0[k] - \frac{\theta_p^0[k]-\theta_p^{100}[k]}{\theta_n^{100}[k]-\theta_n^0[k]}(\theta_n - \theta_n^0[k])$ and $\theta_p(\theta_n)\big|_k = \theta_p\big(\theta_n + \Delta\theta_n^{loss}[k]\big)\big|_{k-1}$.

The first expression is derived from the relationships between $z[k]$ and $\theta_n[k]$ (Eq. (6)) and the equivalent relationship between $z[k]$ and $\theta_p[k]$, which is:

$$z[k] = \frac{\theta_p^0[k] - \theta_p[k]}{\theta_p^0[k] - \theta_p^{100}[k]} \tag{A.1}$$

Generalizing Eqs. (6) and (A.1) for any value inside the corresponding domains: $z \in [0,1] \leftrightarrow \theta_n \in \left[\theta_n^0[k], \theta_n^{100}[k]\right] \leftrightarrow \theta_p \in \left[\theta_p^{100}[k], \theta_p^0[k]\right]$, provides the relationship between the variables (rather than between specific points) at instant k:

$$z(\theta_n)\big|_k = \frac{\theta_n - \theta_n^0[k]}{\theta_n^{100}[k] - \theta_n^0[k]} \tag{A.2}$$

$$z\big(\theta_p\big)\big|_k = \frac{\theta_p^0[k] - \theta_p}{\theta_p^0[k] - \theta_p^{100}[k]} \tag{A.3}$$

Equaling right hand sides of Eqs. (A.2) and (A.3) and solving for θ_p results in the first expression of Eq. (27), which is reproduced next, introducing the coefficient $C_{pn} = \frac{\theta_p^0[k]-\theta_p^{100}[k]}{\theta_n^{100}[k]-\theta_n^0[k]}$, which relates θ_p to θ_n, to simplify notation:

$$\theta_p(\theta_n)\big|_k = \theta_p^0[k] - C_{pn}(\theta_n - \theta_n^0[k]) \tag{A.4}$$

This coefficient is proven to be constant next. This is derived from the fact that the total amount of cyclable lithium at any given instant, $n_{Li}^{cyclable}[k]$ (in mol), is exactly the same for both the PE and the NE –in fact, $n_{Li}^{cyclable}[k]$ is shared between both electrodes. From the definition of θ_p and θ_n, $\left(\theta_p^0[k] - \theta_p^{100}[k]\right) = \frac{n_{Li}^{cyclable}[k]/\varepsilon_{s,p}Vol_p}{c_{s,p}^{max}}$, and $(\theta_n^{100}[k] - \theta_n^0[k]) = \frac{n_{Li}^{cyclable}[k]/\varepsilon_{s,n}Vol_n}{c_{s,n}^{max}}$. Therefore:

$$n_{Li}^{cyclable}[k] = \varepsilon_{s,p}Vol_p c_{s,p}^{max}(\theta_p^0[k] - \theta_p^{100}[k]) = \varepsilon_{s,n}Vol_n c_{s,n}^{max}(\theta_n^{100}[k] - \theta_n^0[k]) \tag{A.5}$$

from where C_{pn} is calculated:

$$C_{pn} = \frac{\theta_p^0[k] - \theta_p^{100}[k]}{\theta_n^{100}[k] - \theta_n^0[k]} = \frac{\varepsilon_{s,n}Vol_n c_{s,n}^{max}}{\varepsilon_{s,p}Vol_p c_{s,p}^{max}} \qquad \forall\, k \tag{A.6}$$

The second expression in Eq. (27) is derived next from examination of Eqs. (18), (19), together with Eq. (A.4). First, combination of Eq. (18) with Eq. (8) results:

$$\theta_n[k] = \theta_n[k-1] - \frac{i_{app}[k]/Vol_n}{\varepsilon_{s,n}\,F c_{s,n}^{max}}\Delta t + \frac{J_{side}[k]}{\varepsilon_{s,n}\,F c_{s,n}^{max}}\Delta t,$$

which, in turn, combined with Eqs. (21) and (26) results:

$$\theta_n[k] = \theta_n[k-1] - \frac{i_{app}[k]/Vol_n}{\varepsilon_{s,n}\,F c_{s,n}^{max}}\Delta t - \Delta\theta_n^{loss}[k] \tag{A.7}$$

Eq. (19) is reproduced here for clarity:

$$\theta_p[k] = \theta_p[k-1] + \frac{i_{app}[k]/Vol_p}{\varepsilon_{s,p}\,F c_{s,p}^{max}}\Delta t$$

Substituting the term $\theta_p[k-1]$ with Eq. (A.4) specialized at $k-1$ results:

$$\theta_p(\theta_n[k])\big|_k = (\theta_p^0[k-1] - C_{pn}(\theta_n[k-1] - \theta_n^0[k-1])) + \frac{i_{app}[k]/Vol_p}{\varepsilon_{s,p}\,F c_{s,p}^{max}}\Delta t$$

where the term $\frac{i_{app}[k]/Vol_p}{\varepsilon_{s,p}\,F c_{s,p}^{max}}\Delta t = C_{pn}\left(\frac{i_{app}[k]/Vol_n}{\varepsilon_{s,n}\,F c_{s,n}^{max}}\Delta t\right)$ can be expressed in terms of Eq. (A.7):

$$\theta_p(\theta_n[k])\big|_k = (\theta_p^0[k-1] - C_{pn}(\theta_n[k-1] - \theta_n^0[k-1])) + C_{pn}(\theta_n[k-1] - \theta_n[k] - \Delta\theta_n^{loss}[k]),$$

which, rearranged, is:

$$\theta_p(\theta_n[k])\big|_k = \theta_p^0[k-1] - C_{pn}\big(\theta_n[k] + \Delta\theta_n^{loss}[k] - \theta_n^0[k-1]\big),$$

which, according to (A.4) is $\theta_p\left(\theta_n[k] + \Delta\theta_n^{loss}[k]\right)\big|_{k-1}$. Therefore:

$$\theta_p(\theta_n[k])\big|_k = \theta_p\left(\theta_n[k] + \Delta\theta_n^{loss}[k]\right)\big|_{k-1} \tag{A.8}$$

Generalizing this expression for any value of θ_n, the second expression of Eq. (27) is finally obtained:

$$\theta_p(\theta_n)\big|_k = \theta_p\left(\theta_n + \Delta\theta_n^{loss}[k]\right)\big|_{k-1}$$

where the domain is such that $\theta_p \in [0,1]$.

REFERENCES

[1] A. Barré, B. Deguilhem, S. Grolleau, M. Gérard, F. Suard, and D. Riu, "A review on lithium-ion battery ageing mechanisms and estimations for automotive applications," J. Power Sources, vol. 241, pp. 680–689, 2013, https://doi.org/10.1016/j.jpowsour.2013.05.040.

[2] M. R. Palacin and A. de Guibert, "Why do batteries fail?," Science (80-.)., vol. 351, no. 6273, pp. 1253292_1–7, Feb. 2016, https://doi.org/10.1126/science.1253292.

[3] D. Lin, Y. Liu, and Y. Cui, "Reviving the lithium metal anode for high-energy batteries," Nat. Nanotechnol., vol. 12, no. 3, pp. 194–206, 2017, https://doi.org/10.1038/nnano.2017.16.

[4] H. Dai, B. Jiang, X. Hu, X. Lin, X. Wei, and M. Pecht, "Advanced battery management strategies for a sustainable energy future: Multilayer design concepts and research trends," Renew. Sustain. Energy Rev., vol. 138, no. October 2020, p. 110480, 2021, https://doi.org/10.1016/j.rser.2020.110480.

[5] G. L. Plett, Battery Management Systems, Volume I: Battery Modeling. Norwood: Artech House Power Engineering, 2015.

[6] J. Song, B. Xiao, Y. Lin, K. Xu, and X. Li, "Interphases in Sodium-Ion Batteries," Adv. Energy Mater., vol. 8, no. 17, p. 1703082, Jun. 2018, https://doi.org/10.1002/aenm.201703082.

[7] S. J. An, J. Li, C. Daniel, D. Mohanty, S. Nagpure, and D. L. Wood, "The state of understanding of the lithium-ion-battery graphite solid electrolyte interphase (SEI) and its relationship to formation cycling," Carbon N. Y., vol. 105, pp. 52–76, 2016, https://doi.org/10.1016/j.carbon.2016.04.008.

[8] F. Holtstiege, P. Bärmann, R. Nölle, M. Winter, and T. Placke, "Pre-Lithiation Strategies for Rechargeable Energy Storage Technologies : Concepts , Promises and Challenges," pp. 1–39, 2018, https://doi.org/10.3390/batteries4010004.

[9] T. Li, X.-Z. Yuan, L. Zhang, D. Song, K. Shi, and C. Bock, Degradation Mechanisms and Mitigation Strategies of Nickel-Rich NMC-Based Lithium-Ion Batteries, vol. 3, no. 1. Springer Singapore, 2020.

[10] A. Wang, S. Kadam, H. Li, S. Shi, and Y. Qi, "Review on modeling of the anode solid electrolyte interphase (SEI) for lithium-ion batteries," npj Comput. Mater., no. February, 2018,

https://doi.org/10.1038/s41524-018-0064-0.

[11] J. Kasnatscheew, T. Placke, B. Streipert, S. Rothermel, R. Wagner, P. Meister, I. C. Laskovic, and M. Winter, "A Tutorial into Practical Capacity and Mass Balancing of Lithium Ion Batteries," J. Electrochem. Soc., vol. 164, no. 12, pp. A2479–A2486, 2017, https://doi.org/10.1149/2.0961712jes.

[12] C. R. Birkl, M. R. Roberts, E. McTurk, P. G. Bruce, and D. A. Howey, "Degradation diagnostics for lithium ion cells," J. Power Sources, vol. 341, pp. 373–386, 2017, https://doi.org/10.1016/j.jpowsour.2016.12.011.

[13] P. M. Attia, S. Das, S. J. Harris, M. Z. Bazant, and W. C. Chueh, "Electrochemical Kinetics of SEI Growth on Carbon Black: Part I. Experiments," J. Electrochem. Soc., vol. 166, no. 4, pp. E97–E106, Feb. 2019, https://doi.org/10.1149/2.0231904jes.

[14] M. B. Pinson and M. Z. Bazant, "Theory of SEI formation in rechargeable batteries: Capacity fade, accelerated aging and lifetime prediction," J. Electrochem. Soc., vol. 160, no. 2, 2013, https://doi.org/10.1149/2.044302jes.

[15] M. M. Kabir and D. E. Demirocak, "Degradation mechanisms in Li-ion batteries: a state-of-the-art review," Int. J. Energy Res., vol. 41, no. 14, pp. 1963–1986, Nov. 2017, https://doi.org/10.1002/er.3762.

[16] J. M. Reniers, G. Mulder, and D. A. Howey, "Review and Performance Comparison of Mechanical-Chemical Degradation Models for Lithium-Ion Batteries," J. Electrochem. Soc., vol. 166, no. 14, pp. A3189–A3200, 2019, https://doi.org/10.1149/2.0281914jes.

[17] Y. Preger, H. M. Barkholtz, A. Fresquez, D. L. Campbell, B. W. Juba, J. Romàn-Kustas, S. R. Ferreira, and B. Chalamala, "Degradation of Commercial Lithium-Ion Cells as a Function of Chemistry and Cycling Conditions," J. Electrochem. Soc., vol. 167, no. 12, p. 120532, 2020, https://doi.org/10.1149/1945-7111/abae37.

[18] A. V. Randall, R. D. Perkins, X. Zhang, and G. L. Plett, "Controls oriented reduced order modeling of solid-electrolyte interphase layer growth," J. Power Sources, vol. 209, pp. 282–288, 2012, https://doi.org/10.1016/j.jpowsour.2012.02.114.

[19] M. Kassem and C. Delacourt, "Postmortem analysis of calendar-aged graphite/LiFePO4 cells," J. Power Sources, vol. 235, pp. 159–171, 2013, https://doi.org/10.1016/j.jpowsour.2013.01.147.

[20] M. T. Lawder, P. W. C. Northrop, and V. R. Subramanian, "Model-Based SEI Layer Growth and Capacity Fade Analysis for EV and PHEV Batteries and Drive Cycles," J. Electrochem. Soc., vol. 161, no. 14, pp. A2099–A2108, 2014, https://doi.org/10.1149/2.1161412jes.

[21] P. Ramadass, B. Haran, P. M. Gomadam, R. White, and B. N. Popov, "Development of First Principles Capacity Fade Model for Li-Ion Cells," J. Electrochem. Soc., vol. 151, no. 2, pp. 196–203, 2004, https://doi.org/10.1149/1.1634273.

[22] D. Lu, M. Scott Trimboli, G. Fan, R. Zhang, and G. L. Plett, "Nondestructive Pulse Testing to Estimate a Subset of Physics-Based-Model Parameter Values for Lithium-Ion Cells," J. Electrochem. Soc., vol. 168, no. 8, p. 080533, 2021, https://doi.org/10.1149/1945-7111/ac1cfa.

[23] D. Lu, M. Scott Trimboli, G. Fan, R. Zhang, and G. L. Plett, “Implementation of a Physics-Based Model for Half-Cell Open-Circuit Potential and Full-Cell Open-Circuit Voltage Estimates: Part I. Processing Half-Cell Data,” J. Electrochem. Soc., vol. 168, no. 7, p. 070532, 2021, https://doi.org/10.1149/1945-7111/ac11a4.

[24] D. Lu, M. Scott Trimboli, G. Fan, R. Zhang, and G. L. Plett, “Implementation of a Physics-Based Model for Half-Cell Open-Circuit Potential and Full-Cell Open-Circuit Voltage Estimates: Part II. Processing Full-Cell Data,” J. Electrochem. Soc., vol. 168, no. 7, p. 070533, 2021, https://doi.org/10.1149/1945-7111/ac11a5.

[25] A. Sancarlos, M. Cameron, A. Abel, E. Cueto, J. L. Duval, and F. Chinesta, “From ROM of Electrochemistry to AI-Based Battery Digital and Hybrid Twin,” Arch. Comput. Methods Eng., vol. 28, no. 3, pp. 979–1015, 2021, https://doi.org/10.1007/s11831-020-09404-6.

[26] Z. Khalik, M. C. F. Donkers, and H. J. Bergveld, “Model simplifications and their impact on computational complexity for an electrochemistry-based battery modeling toolbox,” J. Power Sources, vol. 488, no. May 2020, p. 229427, 2021, https://doi.org/10.1016/j.jpowsour.2020.229427.

[27] X. Li, M. Xiao, and S. Y. Choe, “Reduced order model (ROM) of a pouch type lithium polymer battery based on electrochemical thermal principles for real time applications,” Electrochim. Acta, vol. 97, pp. 66–78, 2013, https://doi.org/10.1016/j.electacta.2013.02.134.

[28] A. Li, M. Ponchant, J. Sturm, and A. Jossen, “Reduced-order electro-thermal battery model ready for software-in-the-loop and hardware-in-the-loop bms evaluation for an electric vehicle,” World Electr. Veh. J., vol. 11, no. 4, pp. 1–16, 2020, https://doi.org/10.3390/wevj11040075.

[29] A. Kamal, “Physical modeling of lithium-ion aging for automotive applications,” PhD Thesis. Michigan Technological University, Houghton, Michigan, 2018.

[30] Z. Geng, S. Wang, M. J. Lacey, D. Brandell, and T. Thiringer, “Bridging physics-based and equivalent circuit models for lithium-ion batteries,” Electrochim. Acta, vol. 372, p. 137829, 2021, https://doi.org/10.1016/j.electacta.2021.137829.

[31] Y. Li, M. Vilathgamuwa, S. S. Choi, T. W. Farrell, N. T. Tran, and J. Teague, “Development of a degradation-conscious physics-based lithium-ion battery model for use in power system planning studies,” Appl. Energy, vol. 248, no. April, pp. 512–525, 2019, https://doi.org/10.1016/j.apenergy.2019.04.143.

[32] M. Safari, M. Morcrette, A. Teyssot, and C. Delacourt, “Multimodal Physics-Based Aging Model for Life Prediction of Li-Ion Batteries,” J. Electrochem. Soc., vol. 156, no. 3, p. A145, 2009, https://doi.org/10.1149/1.3043429.

[33] G. L. Plett, “Algebraic Solution for Modeling SEI Layer Growth,” ECS Electrochem. Lett., vol. 2, no. 7, pp. A63–A65, Apr. 2013, https://doi.org/10.1149/1.004307eel.

[34] G. L. Plett, “Reduced-Order multi-modal model of SEI layer growth for management and control of lithium-ion batteries,” in 2017 IEEE Conference on Control Technology and Applications (CCTA), Kohala Coast, Hawai’i, Aug. 2017, vol. 2017-Augus, pp. 389–395, https://doi.org/10.1109/CCTA.2017.8062493.

[35] X. G. Yang, Y. Leng, G. Zhang, S. Ge, and C. Y. Wang, “Modeling of lithium plating induced aging of lithium-ion batteries: Transition from linear to nonlinear aging,” J. Power Sources, vol. 360, pp. 28–40, 2017, https://doi.org/10.1016/j.jpowsour.2017.05.110.

[36] R. D. McKerracher, J. Guzman-Guemez, R. G. A. Wills, S. M. Sharkh, and D. Kramer, “Advances in Prevention of Thermal Runaway in Lithium-Ion Batteries,” Adv. Energy Sustain. Res., vol. 2, no. 5, p. 2000059, 2021, https://doi.org/10.1002/aesr.202000059.

[37] R. Machado, “Experimental parameter identification of a physics-based model for solid-electrolyte interphase (SEI) layer growth in lithium-ion batteries,” Master’s thesis. University of Colorado Colorado Springs, 2020.

[38] A. M. Colclasure, K. A. Smith, and R. J. Kee, “Modeling detailed chemistry and transport for solid-electrolyte-interface (SEI) films in Li-ion batteries,” Electrochim. Acta, vol. 58, no. 1, pp. 33–43, 2011, https://doi.org/10.1016/j.electacta.2011.08.067.

[39] R. R. Jobman, “Identification of Lithium-Ion-Cell Physics-Model Parameter Values,” PhD Thesis. University of Colorado Colorado Springs, 2016.

[40] K. Kumaresan, G. Sikha, and R. E. White, “Thermal model for a Li-ion cell,” J. Electrochem. Soc., vol. 155, no. 2, pp. 164–171, 2008, https://doi.org/10.1149/1.2817888.

[41] S. Yu, S. Kim, T. Y. Kim, J. H. Nam, and W. Il Cho, “Model prediction and experiments for the electrode design optimization of LiFePo4/graphite electrodes in high capacity lithium-ion batteries,” Bull. Korean Chem. Soc., vol. 34, no. 1, pp. 79–88, 2013, https://doi.org/10.5012/bkcs.2013.34.1.79.

[42] J. Cannarella and C. B. Arnold, “The effects of defects on localized plating in lithium-ion batteries,” J. Electrochem. Soc., vol. 162, no. 7, pp. A1365–A1373, 2015, https://doi.org/10.1149/2.1051507jes.

[43] M. Mastali, M. Farkhondeh, S. Farhad, R. A. Fraser, and M. Fowler, “Electrochemical modeling of commercial LiFePO4 and graphite electrodes: Kinetic and transport properties and their temperature dependence,” J. Electrochem. Soc., vol. 163, no. 13, pp. A2803–A2816, 2016, https://doi.org/10.1149/2.1151613jes.

[44] D. R. Baker and M. W. Verbrugge, “Modeling overcharge at graphite electrodes: Plating and dissolution of lithium,” J. Electrochem. Soc., vol. 167, no. 1, 2020, https://doi.org/10.1149/2.0042001JES.

[45] L. Kraft, J. B. Habedank, A. Frank, A. Rheinfeld, and A. Jossen, “Modeling and simulation of pore morphology modifications using laser-structured graphite anodes in lithium-ion batteries,” J. Electrochem. Soc., vol. 167, no. 1, 2020, https://doi.org/10.1149/2.0062001JES.

[46] A. Rodríguez, G. L. Plett, and M. S. Trimboli, “Improved transfer functions modeling linearized lithium-ion battery-cell internal electrochemical variables,” J. Energy Storage, vol. 20, no. April, pp. 560–575, 2018, https://doi.org/10.1016/j.est.2018.06.015.

[47] Z. Chu, R. Jobman, A. Rodríguez, G. L. Plett, M. S. Trimboli, X. Feng, and M. Ouyang, “A control-oriented electrochemical model for lithium-ion battery. Part II: Parameter identification

based on reference electrode," J. Energy Storage, vol. 27, no. December 2019, p. 101101, 2020, https://doi.org/10.1016/j.est.2019.101101.

[48] S. Yang, C. Zhang, J. Jiang, W. Zhang, L. Zhang, and Y. Wang, "Review on state-of-health of lithium-ion batteries: Characterizations, estimations and applications," J. Clean. Prod., vol. 314, no. February, p. 128015, 2021, https://doi.org/10.1016/j.jclepro.2021.128015.

[49] B. Pan, D. Dong, J. Wang, J. Nie, S. Liu, Y. Cao, and Y. Jiang, "Aging mechanism diagnosis of lithium ion battery by open circuit voltage analysis," Electrochim. Acta, vol. 362, p. 137101, 2020, https://doi.org/10.1016/j.electacta.2020.137101.

[50] W. Xie, R. He, X. Gao, X. Li, H. Wang, X. Liu, X. Yan, and S. Yang, "Degradation identification of LiNi0.8Co0.1Mn0.1O2/graphite lithium-ion batteries under fast charging conditions," Electrochim. Acta, vol. 392, p. 138979, 2021, https://doi.org/10.1016/j.electacta.2021.138979.

[51] R. Zhang, B. Xia, B. Li, L. Cao, Y. Lai, W. Zheng, H. Wang, and W. Wang, "State of the Art of Lithium-Ion Battery SOC Estimation for Electrical Vehicles," Energies, vol. 11, no. 7, p. 1820, Jul. 2018, https://doi.org/10.3390/en11071820.

[52] N. Kotak, P. Barai, A. Verma, A. Mistry, and P. P. Mukherjee, "Electrochemistry-mechanics coupling in intercalation electrodes," J. Electrochem. Soc., vol. 165, no. 5, pp. A1064–A1083, 2018, https://doi.org/10.1149/2.0621805jes.

[53] F. Leng, C. M. Tan, and M. Pecht, "Effect of Temperature on the Aging rate of Li Ion Battery Operating above Room Temperature," Sci. Rep., vol. 5, no. 1, p. 12967, Oct. 2015, https://doi.org/10.1038/srep12967.

[54] D.-I. Stroe, M. Swierczynski, S. K. Kar, and R. Teodorescu, "Degradation Behavior of Lithium-Ion Batteries During Calendar Ageing—The Case of the Internal Resistance Increase," IEEE Trans. Ind. Appl., vol. 54, no. 1, pp. 517–525, Jan. 2018, https://doi.org/10.1109/TIA.2017.2756026.

[55] X. Sui, M. Świerczyński, R. Teodorescu, and D.-I. Stroe, "The Degradation Behavior of LiFePO4/C Batteries during Long-Term Calendar Aging," Energies, vol. 14, no. 6, p. 1732, Mar. 2021, https://doi.org/10.3390/en14061732.

[56] L. von Kolzenberg, A. Latz, and B. Horstmann, "Solid–Electrolyte Interphase During Battery Cycling: Theory of Growth Regimes," ChemSusChem, vol. 13, no. 15, pp. 3901–3910, 2020, https://doi.org/10.1002/cssc.202000867.

[57] S. Das, P. M. Attia, W. C. Chueh, and M. Z. Bazant, "Electrochemical kinetics of SEI growth on carbon black II: Modeling," arXiv, vol. 166, no. 4, 2019, https://doi.org/10.1149/2.0241904jes.

[58] R. Fu, S. Y. Choe, V. Agubra, and J. Fergus, "Development of a physics-based degradation model for lithium ion polymer batteries considering side reactions," J. Power Sources, vol. 278, pp. 506–521, 2015, https://doi.org/10.1016/j.jpowsour.2014.12.059.

[59] X. Kong, G. L. Plett, M. Scott Trimboli, Z. Zhang, D. Qiao, T. Zhao, and Y. Zheng, "Pseudo-two-dimensional model and impedance diagnosis of micro internal short circuit in lithium-ion

cells," J. Energy Storage, vol. 27, no. July 2019, p. 101085, 2020, https://doi.org/10.1016/j.est.2019.101085.

TABLES

Table 1. Nomenclature used in the ESC equivalent circuit (asterisk $*$ indicates variable).

	Parameter / Variable	Value	Unit
C_1	RC # 1 Capacity	26467	F
C_2	RC # 2 Capacity	52082	F
h	SOC-dependent hysteresis state	$*$	$-$
i	Discharge current	$*$	A
$[k]$	Discrete time index	$*$	$-$
M	SOC-dependent hysteresis coefficient	0.0012	V
M_0	Instantaneous hysteresis coefficient	$4.4782 \cdot 10^{-4}$	V
Q	Cell capacity	$*$	Ah
R_0	Initial equivalent series resistance	1.3164	$m\Omega$
R_1	RC # 1 resistance	0.1866	$m\Omega$
R_2	RC # 2 resistance	0.9492	$m\Omega$
R_{SEI}	SEI layer resistance	$*$	Ω
z	State of charge (SOC)	$*$	$-$
Δt	Time interval used in discretization	60	s
η	Coulombic efficiency during charging	99.87	%
γ	Hysteresis time constant	523.8311	$-$
θ_p, θ_n	Degree of lithiation of the positive and the negative electrodes (PE and NE)	$*$	$-$
θ_p^0, θ_n^0	$z = 0$ degree of lithiation of the PE and the NE	$*$	$-$
θ_p^{100}, θ_n^{100}	$z = 1$ degree of lithiation of the PE and the NE	$*$	$-$

Table 2. Nomenclature used in the degradation model.

	Parameter / Variable	Unit
a	Specific area of the porous electrode	m^{-1}
A	Area of the electrode	m^2
c	Lithium concentration	$mol\ m^{-3}$
c^{max}	Maximum lithium concentration in the material	$mol\ m^{-3}$
F	Faraday's constant, 96485	$A\ s\ mol^{-1}$
i_0	Exchange current density	$A\ m^{-2}$
J	Local volumetric current density	$A\ m^{-3}$
k_n	Rate of electrochemical reaction	$A\ m^{2.5}\ mol^{-1.5}$
k_R	SEI resistance increase coefficient	$\Omega\ m^3\ A^{-1}\ s^{-1}$
M_P	Average molecular weight of the SEI layer	$kg\ mol^{-1}$
OCP	Open Circuit Potential	V
R_s	Average radius of the NE's particles	m
R_{SEI}	SEI layer resistance	Ω
R_g	Universal gas constant, 8.314	$J\ mol^{-1}\ K^{-1}$
T	Temperature	K
U^{ref}	Local equilibrium potential	V
Vol	Volume of the electrode	m^3
α_a, α_c	Anodic and cathodic charge transfer coefficients of the electrochemical reaction	$-$
ε	Volume fraction of solid phase in the electrode	$-$
η	Electrochemical reaction overpotential	V
ϕ	Local potential of a phase	V
ρ_P	Average density of the SEI components	$kg\ m^{-3}$
	Subscripts	
e	Electrolyte	
I	Intercalation reaction	

n	Negative electrode (NE)
p	Positive electrode (PE)
s	Solid
$side$	Side reaction (SEI)

Table 3. Parameters of the Panasonic cell.

	Value	Unit	Source
α_n, α_p	0.5	–	[21]
$\alpha_{c,side}$	0.5	–	[18]
A_n	1.2152	m^2	[39]
c_e	2000	$mol\ m^{-3}$	[46]
c_s^{max}	32000	$mol\ m^{-3}$	[45]
$\varepsilon_{s,n}$	0.81	–	estimated
k_n	$2.6473 \cdot 10^{-6}$	$A\ m^{2.5}\ mol^{-1.5}$	averaged [21, 39–45]
R_s	$5 \cdot 10^{-6}$	m	[39]
$\theta_n^0[0]$	0.0093	–	estimated
$\theta_n^{100}[0]$	0.5262	–	estimated
$\theta_p^0[0]$	0.8089	–	estimated
$\theta_p^{100}[0]$	0.4280	–	estimated
Vol_n	$7.29 \cdot 10^{-5}$	m^3	[39]

FIGURE CAPTIONS

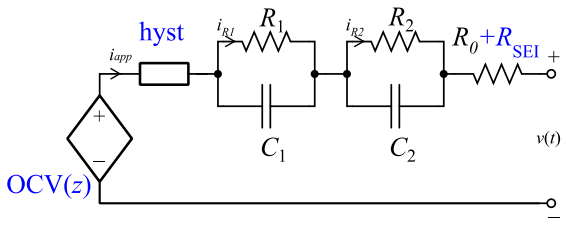

Figure 1. ESC equivalent-circuit model.

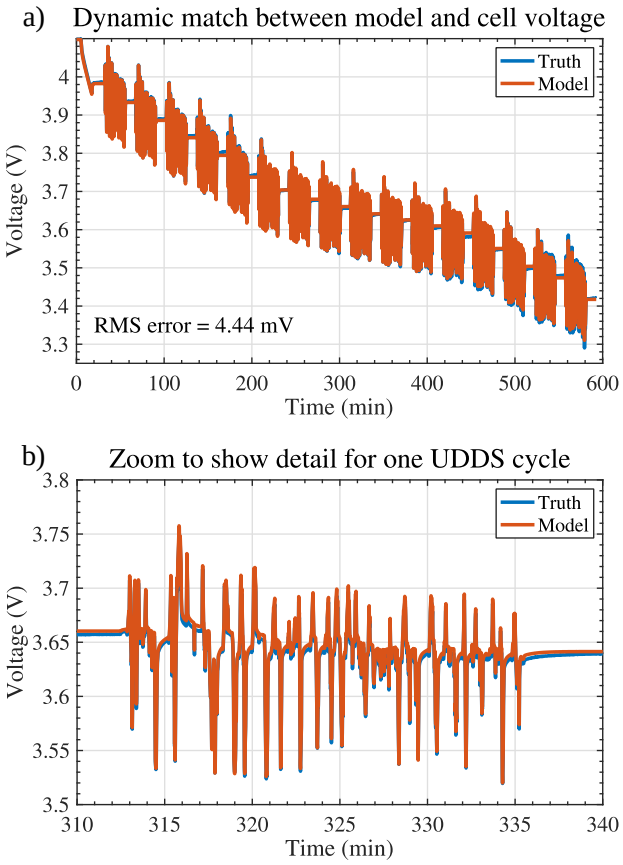

Figure 2. Performance of the ESC model parametrized with the Urban Dynamometer Driving Schedule (UDDS) for electric vehicles: predicted (brown) vs. measured (blue) voltage, a) Full dynamic test; b) Zoom of one UDDS cycle

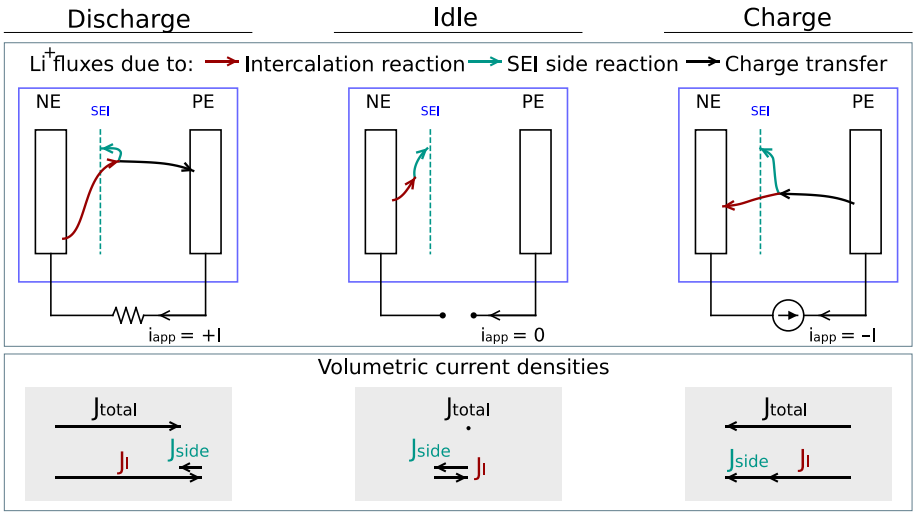

Figure 3. Lithium fluxes and volumetric current densities during cell discharge, inactivity and charge. (NE = Negative Electrode, PE = Positive Electrode.)

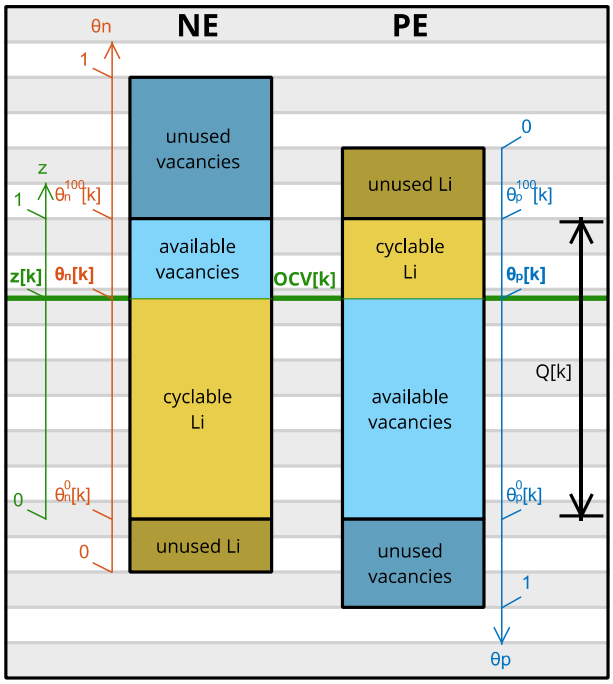

Figure 4. Intuitive representation of PE's and NE's degrees of lithiation θ_p and θ_n as lithiation levels.

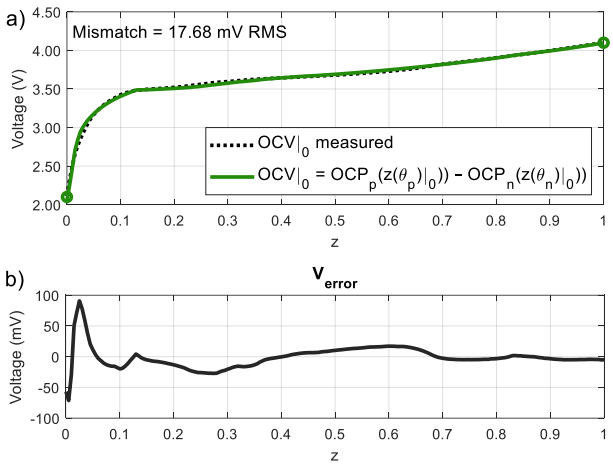

Figure 5. Initial OCV fitting: a) Result of $OCP_p - OCP_n$ best fit to $OCV|_0$; b) Voltage error.

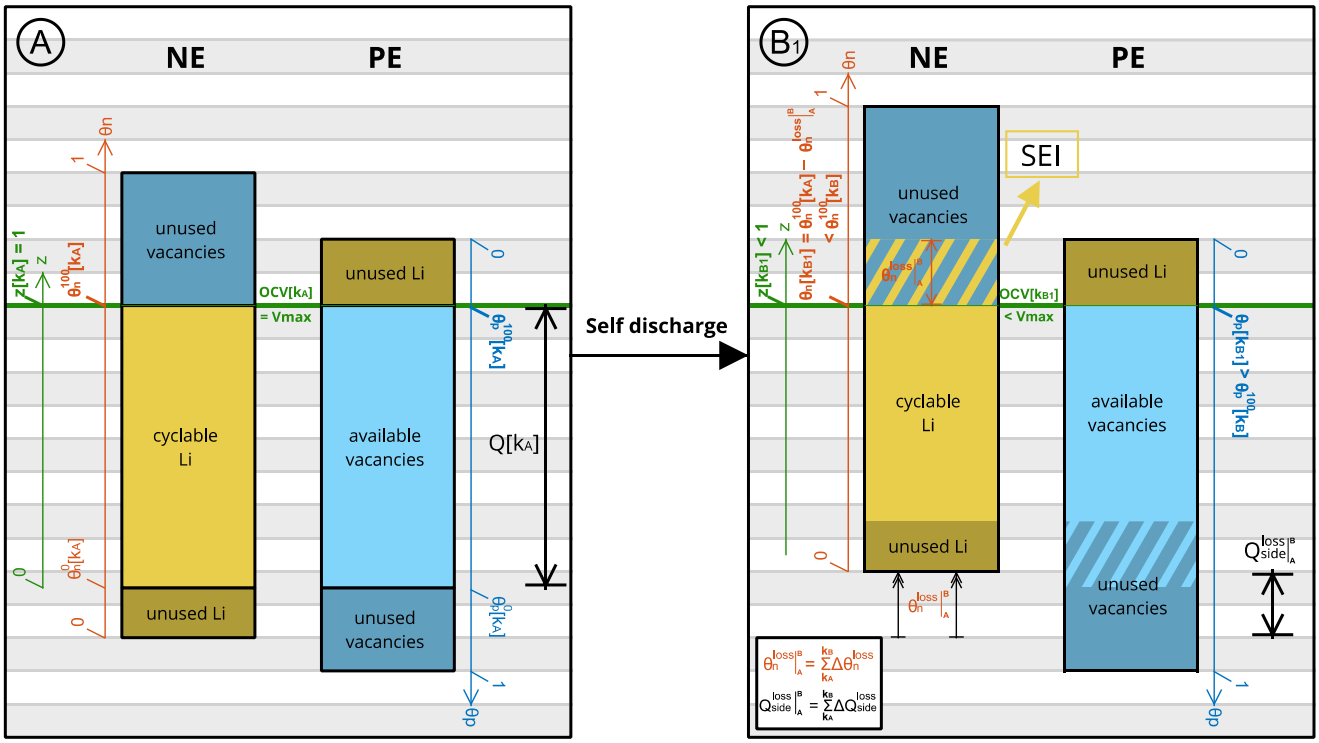

Current degree of lithiation

Current degree of lithiation

NE — Loss of lithium inventory (LLI) due to SEI layer growth

PE — Increase of unused vacancies reserve directly due to LLI (before tuning)

Thought experiment: Full discharge

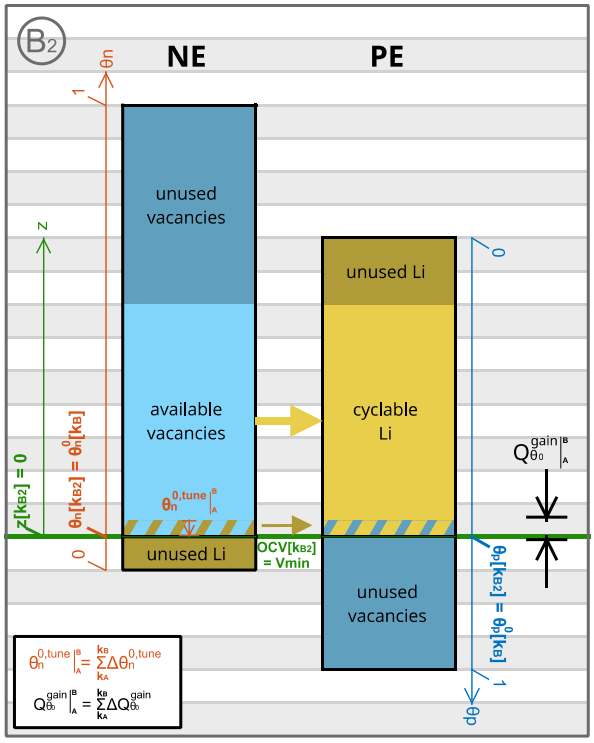

Thought experiment: Full charge

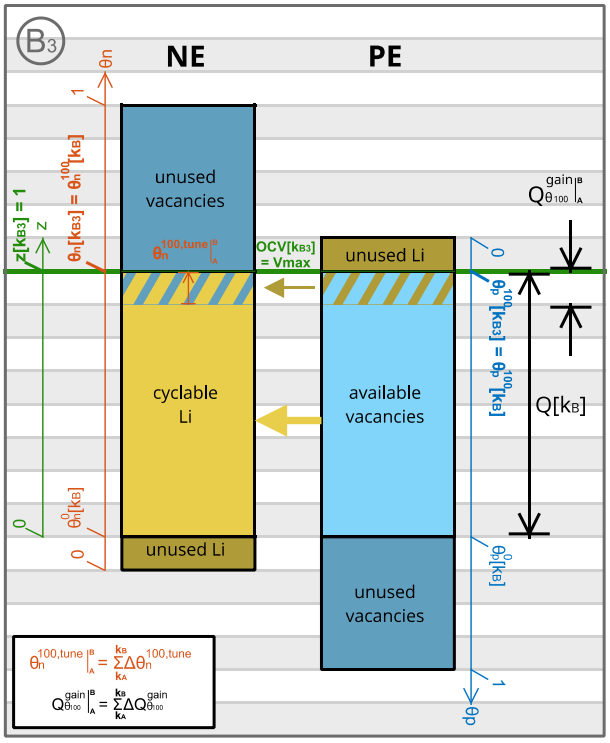

Current degree of lithiation

NE — Surrender of Li to PE

PE — Incorporation of Li from NE reserve

Current degree of lithiation

NE — Incorporation of Li from PE reserve

PE — Surrender of Li to NE

Figure 6. Recalculation of lithiation boundaries in the degraded cell after a self-discharge period. A) Fresh fully-charged cell; B_1) Degraded cell: cyclable lithium has been lost after prolonged self-discharge time $\theta_n^{loss}|_A^B$, and the associated capacity loss is $Q_{side}^{loss}|_A^B$; B_2) Update of θ_p^0 and θ_n^0, and associated capacity recovery $Q_{\theta_0}^{gain}|_A^B$; B_3) Update of θ_p^{100} and θ_n^{100}, and associated capacity recovery $Q_{\theta_{100}}^{gain}|_A^B$. An extended self-discharge period occurs between A) and B_1). The stages in the bottom, B_2) and B_3), are the result of thought experiments consisting in fully discharging and charging the degraded cell until reaching the cut-off voltages V_{min} and V_{max}, respectively.

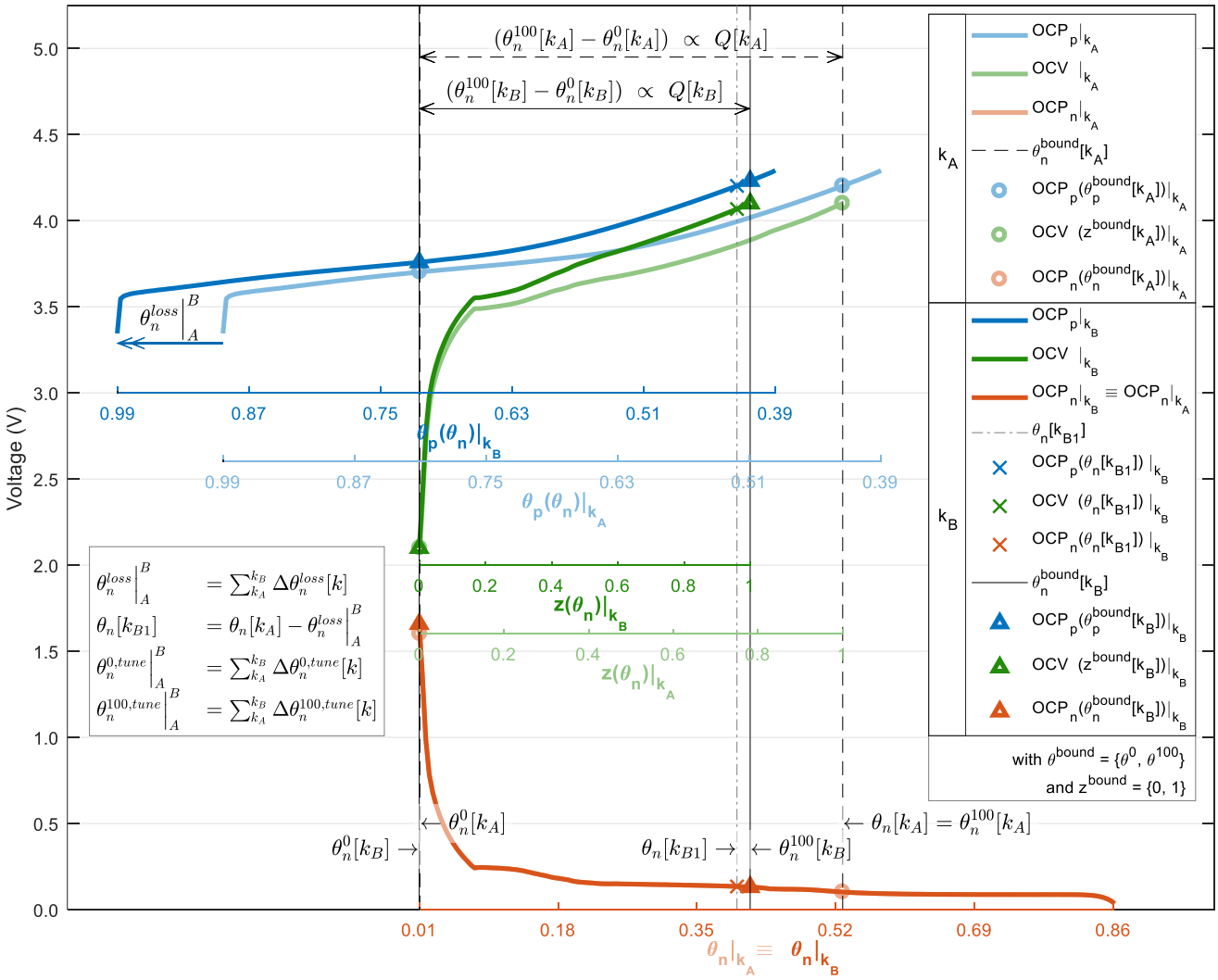

Figure 7. Relative displacement $\theta_n^{loss}\,|_A^B$ between the PE's stoichiometric window θ_p (blue x axis) with respect to the reference, the NE's stoichiometric window θ_n (orange x axis), after an extended period of degradation ($k_A \rightarrow k_B$). Pastel color curves correspond to the initial instant k_A (pre-degradation), and solid color curves correspond to the final instant k_B (post-degradation). The OCP_p curve (blue) gets displaced with respect to OCP_n (orange) and, consequently, OCV (green) gets horizontally shrank.

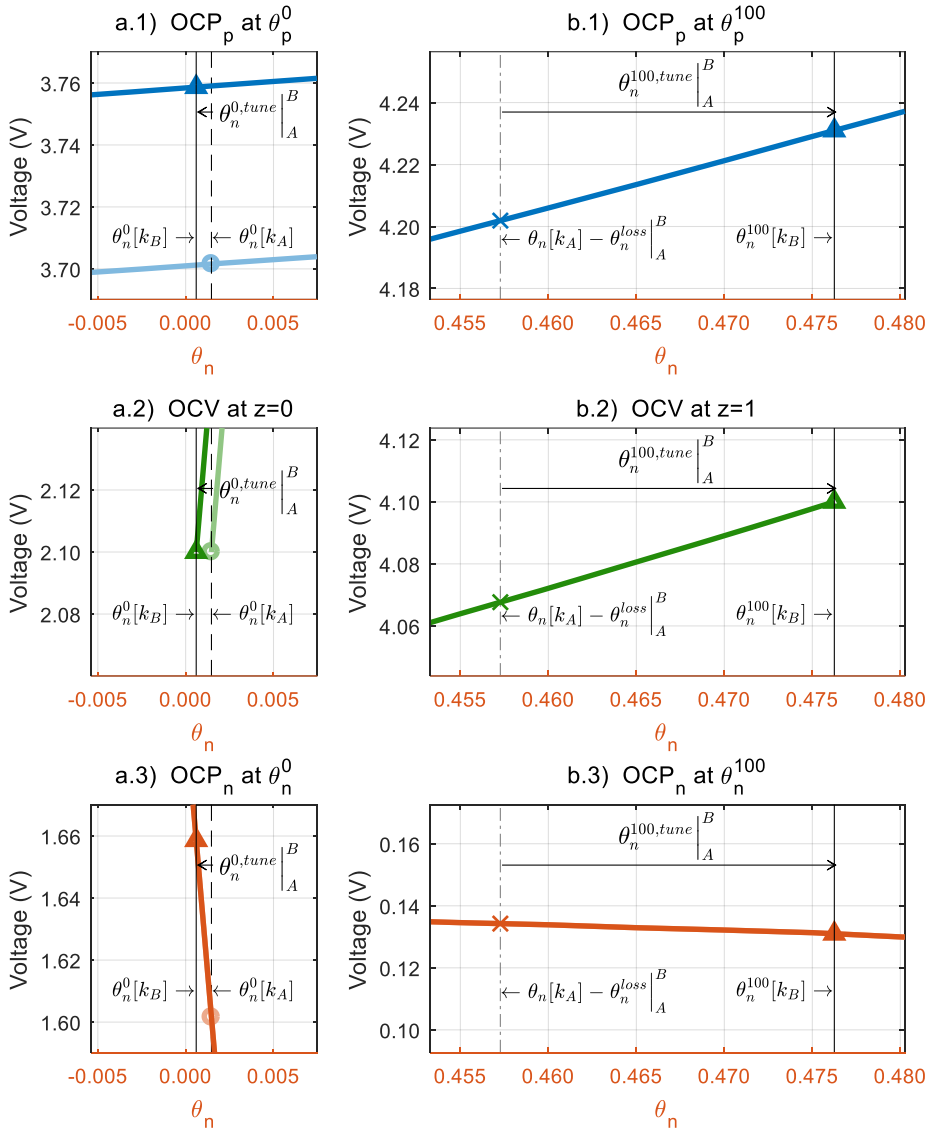

Figure 8. Zooms of Figure 7. Interpretation of $\theta_n^{0,tune}|_A^B$ and $\theta_n^{100,tune}|_A^B$: a) Recalculation of θ_n^0 such that $OCV(\theta_n^0[k_B])\,|_{k_B} = V_{min}$; b) Recalculation of θ_n^{100} such that $OCV(\theta_n^{100}[k_B])\,|_{k_B} = V_{max}$.

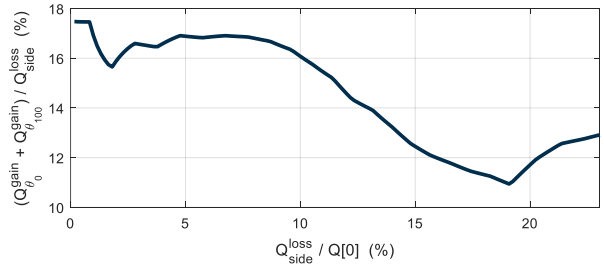

Figure 9. Relative capacity recovery $\left(Q_{\theta_0}^{gain} + Q_{\theta_{100}}^{gain}\right)$ with respect to SEI capacity loss Q_{side}^{loss}.

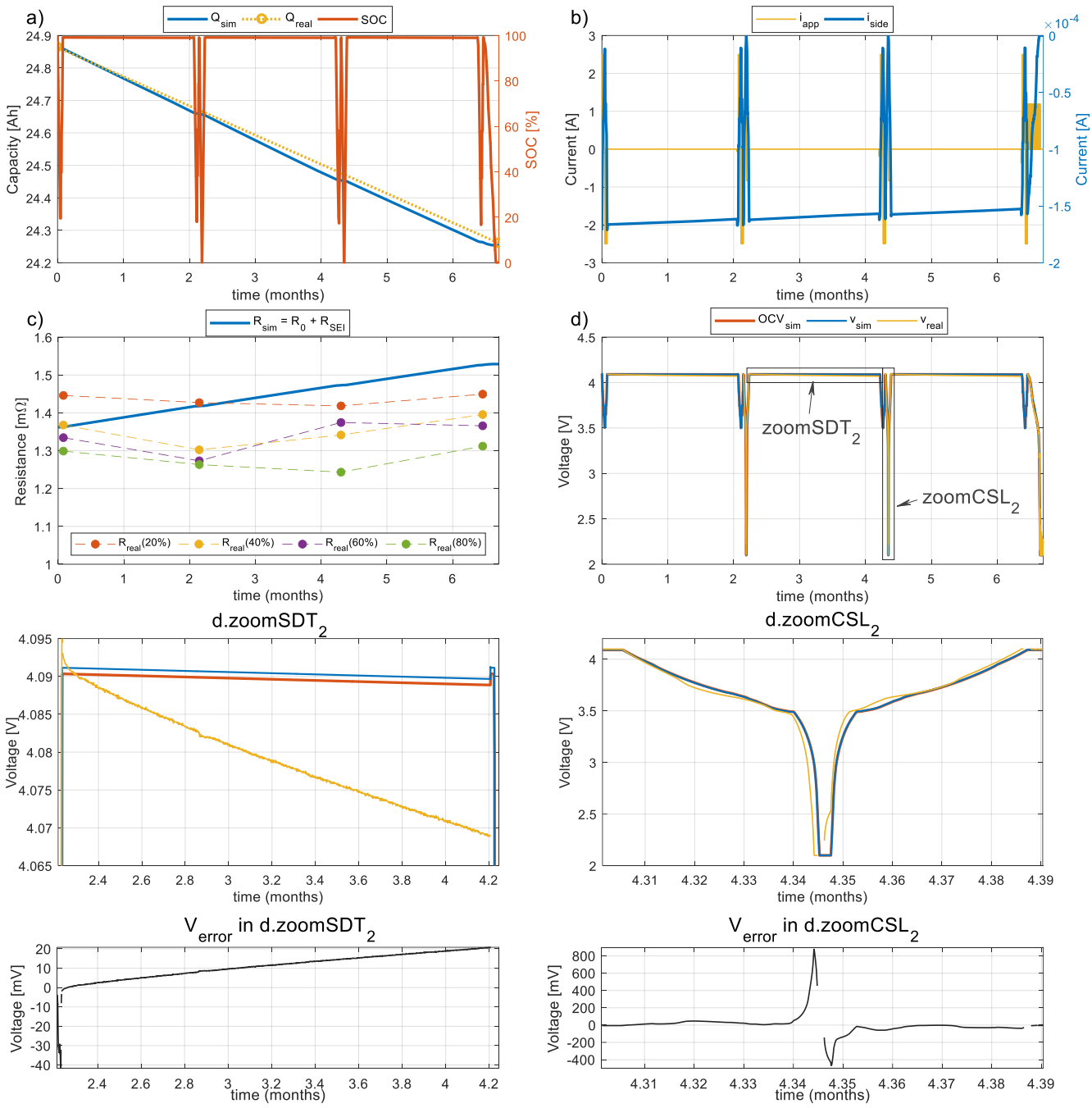

Figure 10. Simulation results: cell response under the application of a current profile coincident with the set of tests described in [37]: a) Capacity and SOC, b) Applied current and SEI side-reaction current, c) Series resistance, d) OCV and cell voltage. Blue and red curves are the simulation results; yellow curves are the real values, measured during testing. The SDT2 and CSL2 regions of d) have been zoomed in to make small disagreement between the model results and real measurements visible and the voltage error has been plotted in the bottom graphs.

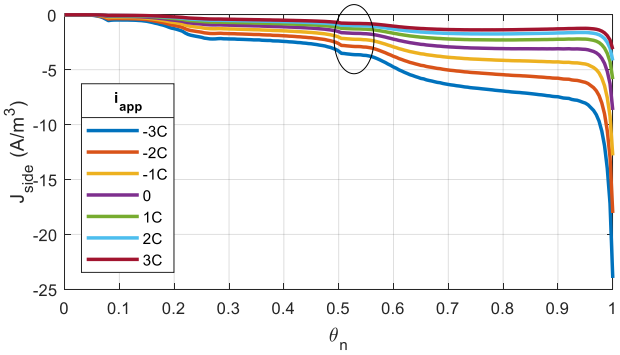

Figure 11. J_{side} dependency on θ_n at various current rates at $T = 25\ °C$.